Ⓔ

Broadband (0–5 Hz) Fully Deterministic 3D Ground-Motion Simulations of a Magnitude 7.0 Hayward Fault Earthquake: Comparison with Empirical Ground-Motion Models and 3D Path and Site Effects from Source Normalized Intensities

by Arthur J. Rodgers, N. Anders Petersson, Arben Pitarka, David B. McCallen, Bjorn Sjogreen, and Norman Abrahamson

ABSTRACT

We report on high-performance computing (HPC) fully deterministic simulation of ground motions for a moment magnitude (M_w) 7.0 scenario earthquake on the Hayward fault resolved to 5 Hz using the SW4 finite-difference code. We computed motions obeying physics-based 3D wave propagation at a regional scale with an M_w 7.0 kinematic rupture model generated following Graves and Pitarka (2016). Both plane-layered (1D) and 3D Earth models were considered, with 3D subsurface material properties and topography interpolated from a model of the U.S. Geological Survey (USGS). The resulting ground-motion intensities cover a broader frequency range than typically considered in regional-scale simulations, including higher frequencies relevant for engineering analysis of structures. Median intensities for sites across the domain are within the reported between-event uncertainties (τ) of ground-motion models (GMMs) across spectral periods 0.2–10 s (frequencies 0.1–5 Hz). The within-event standard deviation ϕ of ground-motion intensity measurement residuals range 0.2–0.5 natural log units with values consistently larger for the 3D model. Source-normalized ratios of intensities (3D/1D) reveal patterns of path and site effects that are correlated with known geologic structure. These results demonstrate that earthquake simulations with fully deterministic wave propagation in 3D Earth models on HPC platforms produce broadband ground motions with median and within-event aleatory variability consistent with empirical models. Systematic intensity variations for the 3D model caused by path and site effects suggest that these epistemic effects can be estimated and removed to reduce variation in site-specific hazard estimates. This study motivates future work to evaluate the validity of the USGS 3D model and investigate the development of path and site corrections by running more scenarios.

Supplemental Content: Animation of ground motions from the 3D subsurface model with topography.

INTRODUCTION

The Hayward fault (HF) dominates seismic hazard in the eastern San Francisco Bay area (SFBA), also referred to as the "East Bay." Currently, the HF and its northern extension, the Rodgers Creek fault, represent the most likely fault in the SFBA to rupture with a moment magnitude (M_w) 6.7 or greater in the next 30 yrs according to the Uniform California Earthquake Rupture Forecast, Version 3 (Field and 2014 Working Group on California Earthquake Probabilities, 2015). Figure 1 shows the area of interest for this study. The HF is capable of earthquakes up to M_w 7.0 and presents significant ground-motion hazard to the heavily populated East Bay cities, including Oakland, Berkeley, Hayward, and Fremont. The last major HF rupture occurred on 21 October 1868 with an M_w 6.8–7.0 event (Toppozada *et al.*, 1981, 2002; Bakun, 1999). Instrumental observations of this earthquake are not available; however, historical triangulation data inform the moment magnitude and fault length (7.0 and 52 km, respectively; Yu and Seagall, 1996). Reported intensities were used to create a ShakeMap for the 1868 event (Boatwright and Bundock, 2008). Modified Mercalli intensities of VII–IX
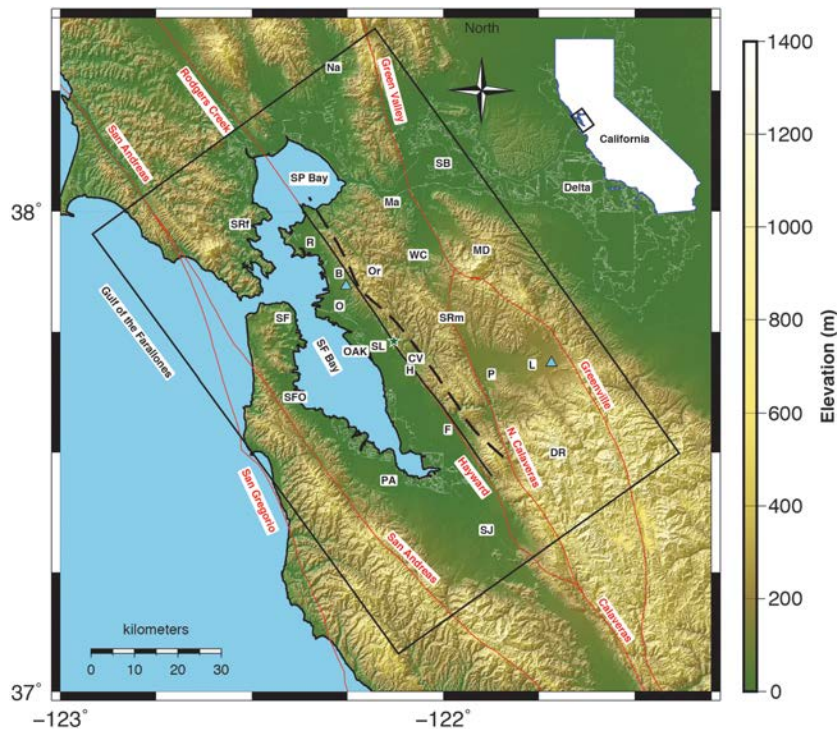
▲ **Figure 1.** Orientation map of the San Francisco Bay area showing the computational domain (rectangle) and major active faults (lines and labels) along with surface topography (bar). The Hayward fault rupture considered is shown with a thick line showing the surface projection of the top of rupture and dashed line for the down-dip edge. City locations are shown: R, Richmond; B, Berkeley; Or, Orinda; O, Oakland; OAK, Oakland Airport; SL, San Leandro; WC, Walnut Creek; Ma, Martinez; CV, Castro Valley; H, Hayward; SRm, San Ramon; F, Fremont; P, Pleasanton; L, Livermore; SJ, San Jose; PA, Palo Alto; SFO, San Francisco Airport; SF, San Francisco; SRf, San Rafael; Na, Napa. Geographic features are also shown: SF Bay, San Francisco Bay; SP Bay, San Pablo Bay; SB, Suisun Bay; MD, Mount Diablo; DR, Diablo Range. Two sites (Oakland and Livermore) where waveforms are shown in Figures 3 and 4 are indicated by the triangles. The location of the domain in the State of California is shown in the inset (upper right). The color version of this figure is available only in the electronic edition.

were experienced near the HF and associated with structural damage in Hayward and Oakland. Recently, Hough and Martin (2015) reanalyzed intensity data in the context of modern felt reports and concluded a lower M_w range of 6.3–6.7 for this event.

2018 marked the 150th anniversary of the 1868 event, and we are currently well within the estimated recurrence interval of large earthquakes on the HF. Paleoseismic evidence indicates that 11 large events occurred on the HF before the 1868 rupture with a recurrence interval of ∼140–160 yrs (Lienkaemper et al., 2002, 2010). Consequently, another damaging HF rupture is more than plausible. Ground motions for a potential large event on the HF are of high interest to residents, governments, and emergency managers as well as earthquake scientists and engineers. Such an event could have dramatic and grave consequences for the nearly 2.5 million residents of Alameda, Contra Costa, and Santa Clara counties and the economy of the region and state.

Simulation of ground motions for another large earthquake on the HF with physics-based fully 3D wave propagation is

timely, particularly with modern computational methods and platforms that enable increased resolution and realism of computed motions. Previous studies computed relatively low-frequency motions (≤1 Hz) with 3D Earth models and wave propagation (Larsen et al., 2000; Harmsen et al., 2008; Aagaard et al., 2010). Recently, our team computed ground motions for HF earthquakes to 2.5 Hz (Johansen et al., 2017) and 4.2 Hz (Rodgers, Pitarka, et al., 2018) with the state-of-the-art SW4 summation-by-parts time-domain finite-difference code and world-class high-performance computing (HPC) resources at the Department of Energy National Laboratories.

Numerical simulation provides a valuable tool for generating earthquake ground motions in 3D Earth models for seismic hazard and risk studies (e.g., Graves et al., 2008; Olsen et al., 2009; Cui et al., 2013). They can provide motions when empirical data are lacking for large events and short distances. Simulated ground-motion time series can be used to analyze the response of engineered structures or geotechnical models (e.g., buildings, bridges, site response, liquefaction, and soil–structure interaction). Advances in numerical methods, computational efficiency, and the inexorable growth in computational power have led to wider use of computed seismic motions for seismic hazard and risk studies. Various methodologies emerged for computing seismic motions in realistic 3D Earth models, including the finite-difference method (e.g., Boore, 1972; Virieux, 1986; Levander, 1988; Vidale and Helmberger, 1988; Olsen et al., 1995; Graves, 1996; Pitarka, 1999; Sjogreen and Petersson, 2012; Cui et al., 2013; Moczo et al., 2014), pseudospectral methods (Furumura et al., 1998; Igel, 1999), finite-element methods (Bao et al., 1998; Tu et al., 2006; Taborda and Bielak, 2011), spectral element methods (Komatitsch and Tromp, 1999; Komatitsch et al., 2005; Chaljub et al., 2007; Peter et al., 2011; Afanasiev et al., 2018), and the discontinuous Galerkin method (Käser and Dumbser, 2005; Dumbser and Käser, 2006; Etienne et al., 2010; Wenk et al., 2013). Although each method may have advantages and disadvantages for any specific problem, comparisons of different methods have proven insightful and have generally improved implementations (Bielak et al., 2010; Chaljub et al., 2010; Moczo et al., 2011).

Simpler methods allow simulation of motions in 1D (plane-layered) media (e.g., semianalytic wavenumber integration, Bouchon, 1981; Zhu and Rivera, 2002) or from the stochastic method (Hanks and McGuire, 1981; Boore, 1983, 2003). Although these methods allow computation of ground motions to high frequency on single processor computers, 3D modeling of wave propagation has the important advantage of

including scattering, mode conversion, and focusing effects caused by material heterogeneity in the Earth (e.g., Vidale and Helmberger, 1988; Olsen, 2000; Hartzell *et al.*, 2010). Motions computed with stochastic Green's function methods cannot represent proper *P*-, *S*-, and surface-wave modes and polarizations. Furthermore, waveforms obtained with these methods at adjacent sites are likely to be uncorrelated even at long periods, which violates wave propagation physics. Motions from a 1D Earth model are likely to be more spatially correlated than those from a 3D model because lateral homogeneity and a lack of scattering maintain coherence of the computed wavefield. Hybrid methods combine deterministic motions for low frequencies from either 1D or 3D modeling with high-frequency motions from the stochastic method with a transition frequency around 1 Hz. Motions from hybrid methods suffer from not including the effects of wave propagation in realistic 3D Earth models across a broad frequency band or from the vagaries of stochastic motion at high frequencies. Accounting for path- and site-specific intensity corrections to ground-motion models (GMMs) is important for improving hazard estimates (Anderson and Brune, 1999). Recent analysis of spectral correlation properties of ground motions suggests the stochastic method generates less correlation between amplitudes at different frequencies compared to observed motions, which impacts building response and risk (Stafford, 2017; Bayless and Abrahamson, 2018).

3D numerical simulation of wave propagation results in more realistic motions obeying wave propagation physics. However, 3D modeling is computationally intensive: each doubling of the maximum resolved frequency (f_{max}) requires halving the grid spacing or mesh element size in three dimensions as well as a halving of the timestep. This results in a factor of 16 (2^4) increase in the computational effort to double f_{max} for a given domain and seismogram duration. Path and site effects result from wave propagation in the heterogeneous 3D Earth, and these phenomena have been studied with physics-based wave propagation modeling (Kawase, 1996; Graves *et al.*, 1998; Olsen *et al.*, 2006; Day *et al.*, 2008; Frankel *et al.*, 2009). Running simulations on HPC platforms is necessary for resolution of higher frequencies, particularly those of relevance to engineering analysis (well above 1 Hz). Although low-frequency (up to 1 Hz or higher in some cases) waveform simulations with 3D models have shown promise fitting waveforms from moderate earthquakes (e.g., Rodgers *et al.*, 2008; Taborda and Bielak, 2013; Taborda *et al.*, 2016), the extension of simulations to compute higher frequency motions and improvement of source and Earth models to fit higher frequencies remains a current challenge in seismology. Unfortunately, 3D seismic models based on geologic and geophysical data cannot consistently fit details of observed waveforms particularly for higher frequencies (>1 Hz), and this motivates improvement of models with waveform inversion (e.g., Tape *et al.*, 2009). However, there is still value in computing the higher frequency 3D response to large earthquake forcing to evaluate the extent to which engineering ground-motion intensity measurements (GMIMs) can be predicted with current models. For the SFBA, the U.S. Geological Survey (USGS) 3D geologic and seismic model (USGS, 2018) represents the current best estimate of subsurface structure for the region, although comparisons with observed moderate earthquake ground motions reveal strengths and shortcomings of the model (Rodgers *et al.*, 2008; Aagaard *et al.*, 2010; Kim *et al.*, 2010).

In this study, we describe ground-motion simulations for an M_w 7.0 HF earthquake resolved to 5 Hz using fully 3D wave propagation. We note that this is a higher resolved frequency than previous studies in northern California. The simulation was made possible with advances in the underlying finite-difference methodology and computational algorithms as well as access to and optimization for the Cori Phase-II supercomputer at Lawrence Berkeley National Laboratory (LBNL). The computed motions provide new data to evaluate seismic ground-motion hazard and risk in the SFBA, particularly near the HF and the East Bay. Below, we describe the SW4 code, the computational setup, and the resulting ground motions. Analysis of the validity of computed motions is performed by comparing GMIMs to GMMs. We found good agreement of the GMIMs with GMMs from the Pacific Earthquake Engineering Research Center (PEER) Next Generation Attenuation-West2 project (NGA-West2). We also introduce the concept of source normalization to show how 3D structure results in path and site effects that are correlated with known geologic structure. We then discuss the implications of this effort and next steps toward fully 3D HPC simulation of damaging earthquake ground motions for hazard and risk, with emphasis on path and site effects.
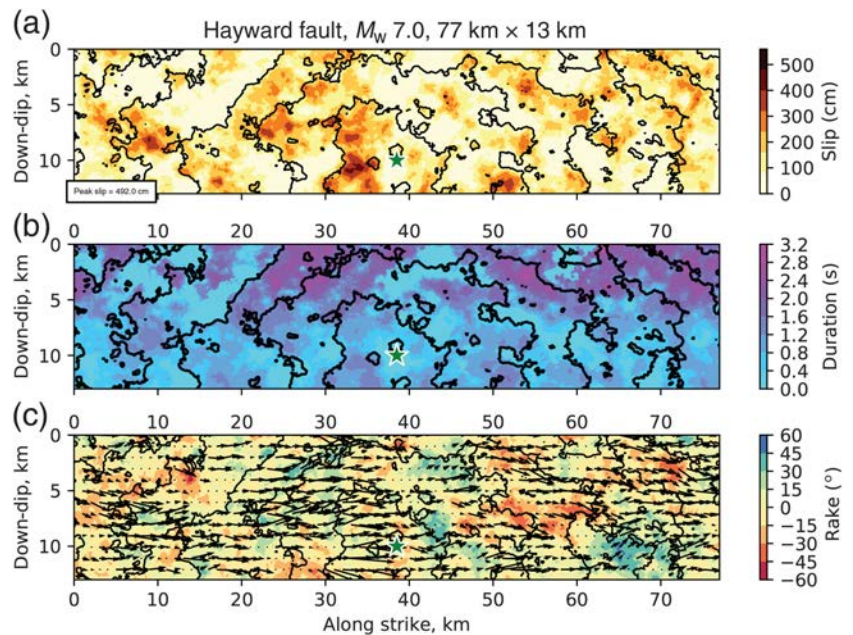
SW4 SIMULATIONS

SW4 is a time-domain fourth-order accurate finite-difference code based on the summation-by-parts principle for accurate and efficient simulation of seismic wave propagation (Petersson and Sjögreen, 2012, 2014, 2015; Sjogreen and Petersson, 2012). It solves the elastodynamic equations of motion for an anelastic solid with 3D variations in material properties and surface topography. SW4 has many desirable features for earthquake simulations, including fully 3D material properties including anisotropy, anelastic attenuation with *P*- and *S*-wave quality factors, surface topography with a near-surface curvilinear mesh, and depth-dependent mesh refinement as seismic wavespeeds increase and supergrid absorbing boundary conditions. One of the most effective features of SW4 is its built-in curvilinear mesh generator, which automatically creates the grid from the user-supplied topography at runtime startup. SW4 has been verified against canonical problems, including canonical 1D problems and 3D material models with the method of manufactured solutions (Petersson and Sjogreen, 2018).

SW4 and its second-order predecessor WPP (Nilsson *et al.*, 2007; Petersson and Sjogreen, 2010) have been used for earthquake (Aagaard *et al.*, 2008, 2010; Rodgers *et al.*, 2008; Dreger *et al.*, 2015; Johansen *et al.*, 2017; Rodgers, Pitarka, *et al.*, 2018) and explosion ground-motion simulations (Rodgers *et al.*, 2010; Pitarka *et al.*, 2015; Hirakawa *et al.*, 2016). Under a recent

Department of Energy Exascale Computing Project, SW4 has been modified to improve efficiency on computers with many cores (central processing units [CPUs]) per node with a hybrid OpenMP–message passing interface (MPI) parallelization scheme. The simulations described here were performed on the Cori Phase-II cluster at the National Energy Resources Scientific Computing (NERSC) Center at LBNL, which has 68 cores (CPUs) per node and 9688 total nodes. Within each node, shared memory allows efficient multithreaded execution of loops without the need to explicitly pass ghost point values after each timestep, as is needed between MPI tasks. We found that two OpenMP threads per MPI tasks perform optimally on this architecture. For the 3DTOPO calculation (described later), we used 8192 nodes with 32 MPI tasks per node and 2 OpenMP threads per MPI task. The 1DFLAT calculation (described later) with higher minimum shear wavespeed $V_{S\,\mathrm{min}}$, and larger grid spacing required only 600 nodes but used the same hybrid OpenMP–MPI scheme. On each node, 4 cores were dedicated to the operating system, leaving 64 cores per node for the SW4 simulation. Throughput of data to disk was improved using Cori-II's Burst Buffer, which enabled 5 TB checkpoint files to be written in less than 50 s (109 GB/s).

▲ **Figure 2.** Magnitude 7.0 earthquake rupture generated by the method of Graves and Pitarka (2010, 2015, 2016). The panels show (a) slip, (b) duration, and (c) rake. The hypocenter is indicated by the star. Contours of rupture time (interval 3.0 s) are shown in each panel. Rake vectors are shown along with shade coding in (c). The color version of this figure is available only in the electronic edition.

COMPUTATIONAL DOMAIN, EARTH, AND RUPTURE MODELS

We used a regional-scale domain that spanned 120×80 km laterally and 35 km in depth. This size was needed to encapsulate the M_w 7.0 rupture and compute the strong near-fault ground motions throughout the greater SFBA. Figure 1 shows the domain in map view along with the surface projection of the rupture model, major active faults, and geographic locations. The rupture area was computed using the simplified scaling relationship of Kamai *et al.* (2014), in which the area in square kilometers A follows $\log_{10} A = M_\mathrm{w} - 4$. The depth to the top-of-rupture z_TOR was set to 1 km below sea level. Future investigations could explore the sensitivity of shaking intensity to this parameter and possible creep on the fault. The down-dip fault width was set to 13 km to span the seismogenic depths (Waldhauser and Ellsworth, 2002; Hardebeck *et al.*, 2007; Waldhauser and Schaff, 2008). The rupture dimensions are 77 km along strike and 13 km down dip and the sense of motion predominantly right-lateral strike slip. The rupture is generated with the slip distribution as a random variable governed by magnitude-dependent correlation structure embedded in the method following Graves and Pitarka (2010, 2015, 2016). The rupture was created for a planar fault approximately following the segment shown in Figure 1. The rupture was then draped onto the HF geometry specified by the USGS 3D model

(USGS, 2018). It is important to honor the fault geometry and the material discontinuity present across the HF in the USGS 3D model. The fault dips at most about 75° to the northeast and is more vertical in the north and less so in the south (Fig. 1). The impact of the fault dip on ground motions near the HF is the subject of another study (Rodgers *et al.*, 2019). We discretized the fault with more than 100,000 subfault patches with dimensions 100×100 m. The slip distribution, duration, and rake on subfault patches are shown in Figure 2. The slip duration increases with the slip amplitude, and the duration also increases for a given slip amplitude in the shallower parts of the fault as specified by Graves and Pitarka (2010, 2015, 2016). The hypocenter was chosen to be located near the San Leandro Salient, where the HF shows some geometric complexity and focal mechanisms that suggest a possible fault segment boundary (Waldhauser and Ellsworth, 2002; Hardebeck *et al.*, 2007). Bakun (1999) and Hough and Martin (2015) suggested the 1868 rupture initiated near this point.

We considered two earth models: a 1D plane-layered average model for the SFBA without topography (1DFLAT), similar to Kamai *et al.* (2014), and the USGS 3D model (USGS, 2018) with topography (3DTOPO). Waveforms were sampled on the ground surface throughout the domain on a 2-km grid. The two calculations were performed with the same domain, time duration (90 s), rupture model, and station geometry. The 1DFLAT and 3DTOPO models had minimum shear wavespeeds of 800 and 500 m/s, respectively. For the 1DFLAT model, a $V_{S\,\mathrm{min}}$ of 800 m/s represents an average hard-rock near-surface crustal structure. For the 3DTOPO model, we

used a $V_{S\,min}$ of 500 m/s as a compromise to distinguish the sedimentary basins from the hard-rock geology at the surface while allowing simulation of high frequencies well above 1 Hz. Strictly speaking, low wavespeeds associated with weak soils (say $V_{S\,min} < 500$ m/s) may experience nonlinear deformation during strong-motion forcing (Hartzell *et al.*, 2004; Bonilla *et al.*, 2005; Pitarka *et al.*, 2013). SW4 does not currently model nonlinear soil response. Both simulations resolved waves with frequencies up to 5 Hz and wavelengths as small as 100 m for the 3DTOPO case using eight points per minimum wavelength. The 3DTOPO simulation used a grid spacing of 12.5 m near the surface and required a total of nearly 25.9 billion grid points. SW4 uses a raster file (rfile, see Petersson and Sjogreen, 2018) version of the USGS (2018) 3D model of the SFBA. SW4 can rapidly read and interpolate the model in parallel while rendering the material properties onto the computational mesh.

Without mesh refinement, the 3DTOPO calculation would have required nearly seven times more grid points (>172 billion) and four times more timesteps to compute the same response. Such a calculation would require even more computational resources (e.g., memory, cores, nodes, and run time) than the Cori Phase-II cluster can provide. SW4's mesh refinement feature is a key to enabling this calculation on the available computing platform. Finite-element and spectral-element methods and mesh generation algorithms such as those in the Hercules (Tu *et al.*, 2006; Taborda and Bielak, 2013) and SPECFEM3D packages (Komatitsch and Tromp, 1999; Chaljub *et al.*, 2007; Peter *et al.*, 2011) allow a similar approach with mesh elements getting larger with depth as seismic wavespeeds increase.

RESULTS

To illustrate the computational effort required to simulate regional-scale ground motions to 5 Hz and the impact on the computed response, we show the resulting ground motions computed in the 3D model with a range of grid spacings and resolved f_{max} at two locations (Oakland and Livermore, indicated in Fig. 1). Each panel in Figure 3 shows the resulting fault-normal acceleration time histories resolved to 0.3125, 0.625, 1.25, 2.5, and 5.0 Hz (minimum grid spacing of 200, 100, 50, 25, and 12.5 m, respectively). The calculations were done for the 3DTOPO model with minimum shear wavespeed, $V_{S\,min} = 500$ m/s. To double the frequency content of the waveforms, the calculations need a factor of 16 more computational effort. Thus, the four frequency doublings shown in Figure 3 to resolve motions from 0.3125 to 5 Hz required 16^4 or 65,536 times more computational effort.

The acceleration amplitudes increase as the resolved frequency increases for both the near fault (Oakland at 2.6 km) and farther station (Livermore at 37.6 km). The amplitude at the near-fault site in Oakland shows a dramatic increase from 2.5 to 5.0 Hz, suggesting different intensity and damage for these two time histories with different resolutions. This is likely because of the nearby deep slip patch with short rise time (i.e., high stress drop) immediately below the site. The response in

Livermore (37.6 km) exhibits long-duration motions. The later arriving converted and/or scattered waves (coda) in Livermore show several arrivals that are predominantly long period but include impulsive onsets at 5 Hz, comparable to or larger than earlier direct arrivals.

Many simulations of ground motions from damaging earthquakes in 3D Earth models resolve motions to about 1 Hz (e.g., Aagaard *et al.*, 2008, 2010). Hybrid methods often use 3D simulations resolved to about 1 Hz and 1D Green's functions or stochastic method time series above 1 Hz (e.g., Pitarka *et al.*, 2000; Crempien and Archuleta, 2015; Olsen and Takedatsu, 2015; Graves and Pitarka, 2016). The 5-Hz time histories shown in Figure 3 and considered herein for the entire computational domain are based on deterministic 3D wave propagation modeling with SW4 and include wave scattering, basin amplification, and mode conversion that hybrid methods can only represent through crude approximations. This is a major advantage of this study and 3D broadband simulations in general. We further explore how 3D structure shapes the response across the 0- to 5-Hz frequency band below.

An animation of the ground motions for the 3DTOPO case is available in the Ⓔ supplemental content to this article. This shows the magnitude of the ground velocity for the 90-s duration of the simulation. Strong path and site effects can be seen leading to asymmetries in the wavefield across the fault. In particular, the sedimentary basins show amplified and long-duration waves (San Pablo Bay, San Leandro basin, Pleasanton-Livermore Valley, and Santa Clara Valley composed of the Evergreen and Cupertino basins).

Ground velocity time series were output on a 2-km grid, and these were processed to measure GMIMs. Figure 4 shows the three-component ground acceleration, velocity, and displacements for the 1DFLAT and 3DTOPO models at the same two locations as Figure 3 (Oakland and Livermore Valley). The displacements in Oakland show the expected right-lateral displacement offsets (~20 cm), velocity pulses (several tens of cm/s), and strong accelerations (30% of the acceleration of gravity, *g*) seen in near-fault records from large earthquakes. There are relatively small differences between the 1DFLAT and 3DTOPO models at the near-fault location in Oakland; however, the 3DTOPO case shows more coda. Motions in Livermore are more complex with the 3DTOPO model showing long duration and scattered arrivals coming as late as the end of the calculation (90 s). Pleasanton and Livermore Valleys are composed of moderately deep sediments, and the long duration of motions from the 3D model arises from wave propagation that cannot be captured in 1D or stochastic method synthetics. The Livermore site is also in the forward rupture directivity zone for slip in the southern-central part of the rupture.

We computed the RotD50 (Boore *et al.*, 2006; Boore, 2010) spectral accelerations (SAs) for each station along with the peak acceleration, velocity, and displacement. These were then compared with four GMMs (also referred to as ground-motion prediction equations) from the PEER NGA-West2 Project: Abrahamson *et al.* (2014; hereafter, ASK14); Boore *et al.* (2014; hereafter, BSSA14); Campbell and Bozorgnia
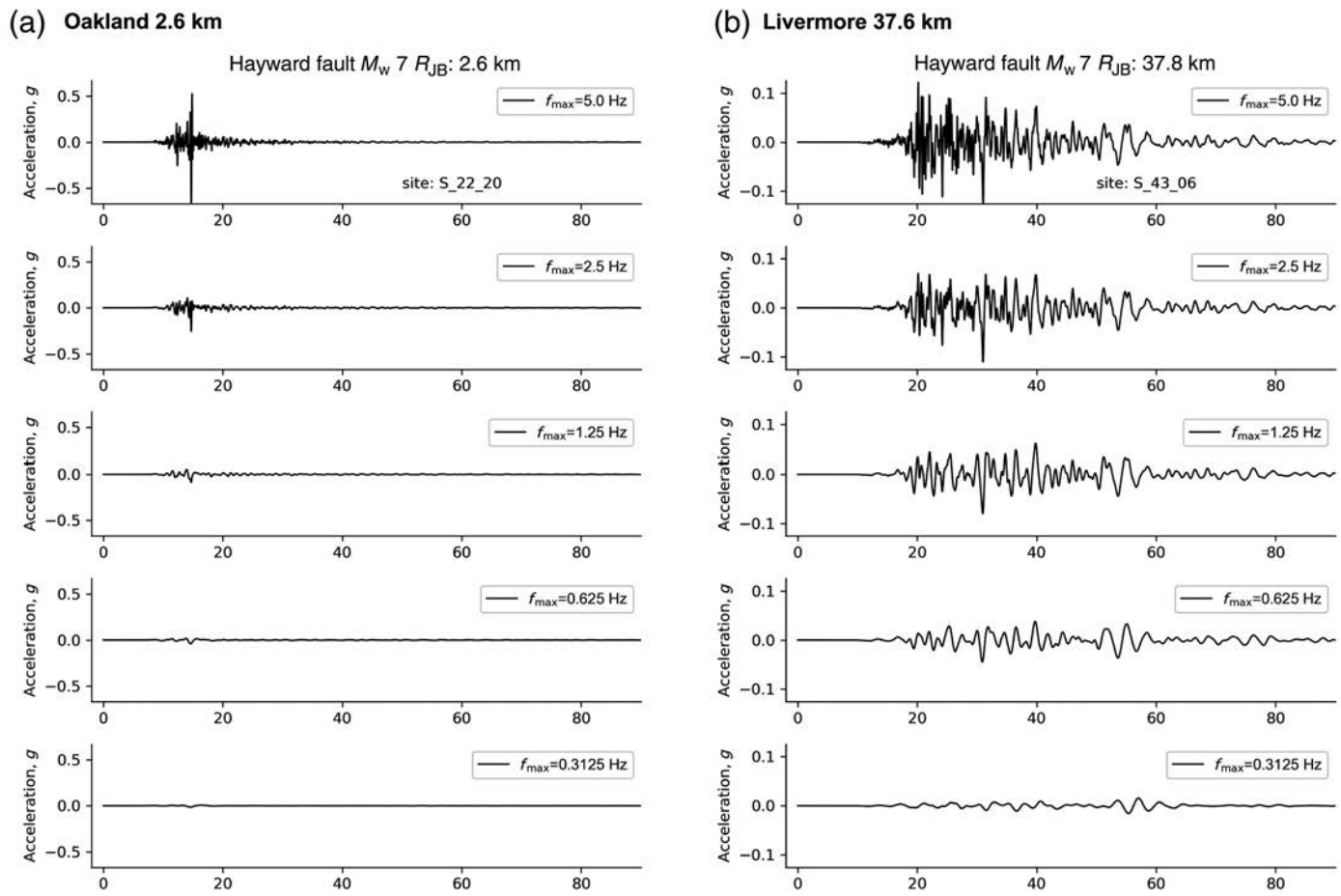
▲ **Figure 3.** Fault-normal ground accelerations for two locations: (a) Oakland and (b) Livermore Valley (both indicated in Fig. 1). Each panel shows the waveforms computed with different maximum resolved frequency, f_{max}: 0.3125, 0.625, 1.25, 2.5, and 5.0 Hz and with the same amplitude scale.

(2014; hereafter, CB14), and Chiou and Youngs (2014; hereafter, CY14). These GMMs use three site-specific terms: V_{S30}, the slowness averaged shear wavespeed of the upper 30 m and $Z_{1.0}$ and $Z_{2.5}$, the depth to the shear wavespeed of 1.0 and 2.5 km/s, respectively. We did not account for directivity effects in the GMMs. The four GMMs give very consistent estimates of the GMIMs.

Examples of RotD50 SAs from simulations are shown in Figure 5 for the same two locations indicated in Figure 1 with waveforms shown in Figure 4. The GMM predictions were computed for the source with path- and site-specific parameters indicated in each panel. The SAs are shown for the full range of GMM predictions, with three orders of magnitude of periods 0.01–10 s (0.1- to 100-Hz frequencies). The minimum resolved period of our simulations (0.2 s) and the poorly resolved short periods (0.01–0.2 s) are indicated for reference. The Oakland site considered for the 1DFLAT and 3DTOPO Earth models (Fig. 5a,c) and the Livermore site for the 1DFLAT model (Fig. 5b) show SAs generally within the 1-σ (total) uncertainties of the GMMs (colored dashed lines). The Livermore site for the 3DTOPO model (Fig. 5d) shows larger motions than predicted by the GMMs for SAs between 1 and 10 s. This is

likely a combination of the forward directivity for slip in the southern portion of the rupture coupling into the sedimentary basins of the Pleasanton and Livermore Valleys. The hard-rock geology of the Diablo Range (Fig. 1) refracts energy back toward these valleys, and this can be seen in the ground-motion animation (Ⓔ Animation S1). Importantly, our band-limited simulations at these sites produce short-period SAs and peak ground accelerations (PGAs, corresponding to the spectral ordinates) that are within the 1-σ uncertainties of the median predictions of GMMs. Short-period SA and PGA are controlled by high-frequency motions, and lower frequency simulations generally cannot produce SA and PGA values consistent with GMMs.

The comparisons shown in Figure 5 consider only two individual sites. To evaluate the performance of the current broad-band 3D simulations, we plot various GMIMs versus Joyner–Boore distance (R_{JB}) and compare them with the ASK14 GMM predictions. Figure 6 shows the PGA, peak ground velocity (PGV), and RotD50 SA at 0.3, 1.0, and 3.0 s versus R_{JB} for the 1DFLAT and 3DTOPO Earth models. In each plot, the ASK14 GMM prediction is plotted with 1-σ uncertainties based on the mean path and site terms. The means, medians, and standard deviations of residuals relative to the ASK14 GMM
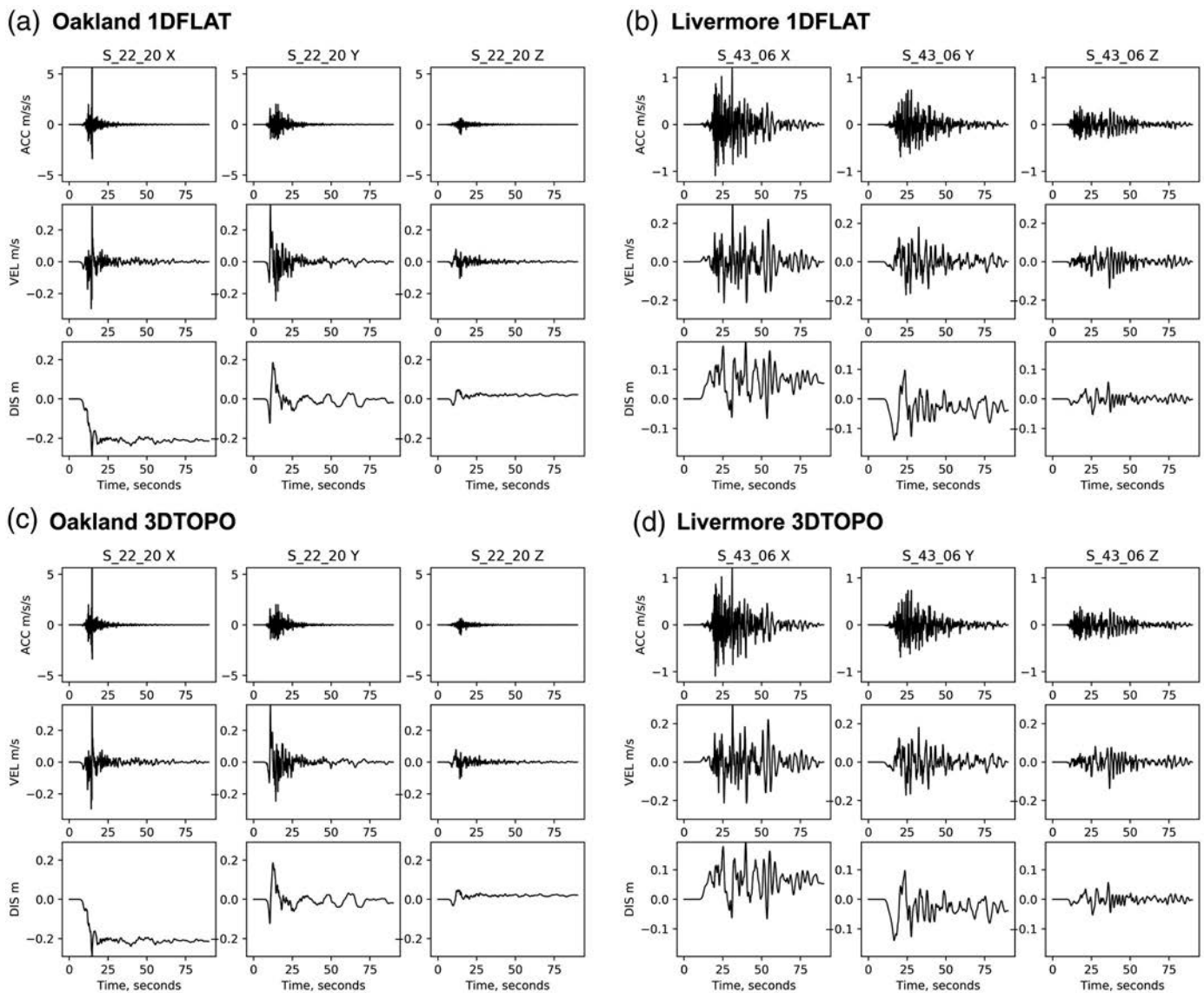
▲ **Figure 4.** Three-component acceleration, velocity and displacements at two locations: Oakland and Livermore Valley (both indicated in Fig. 1). Panels show motions for the 1DFLAT model in (a) Oakland and (b) Livermore and the 3DTOPO model in (c) Oakland and (d) Livermore. Note that in the domain coordinate system, the *X* and *Y* components correspond to fault parallel and normal, respectively.

predictions for the site-specific conditions are given in each panel. The 3DTOPO model consistently produces larger scatter in GMIMs than the 1DFLAT model, which can also be seen in the reported residual statistics shown in each panel. This is no doubt caused by path- and site-specific wave propagation effects (e.g., diffraction, scattering, site and basin amplification, and topographic effects). The symbols in Figure 6 are color coded to indicate the approximate fault-normal distance with red and blue representing locations northeast and southwest of the HF, respectively. The GMIMs for the 1DFLAT Earth model indicate that the motions are slightly higher northeast of the HF relative to locations southwest of the fault. This effect is also seen in the PGV maps from the simulation grid (Fig. 7) and likely caused by the east-dipping nature of the fault.

Maps of the PGV at the resolution of the simulations for the 1DFLAT and 3DTOPO cases are shown in Figure 7. These maps show that a large portion of the SFBA will experience intense shaking compounding emergency response. The 1DFLAT case shows a roughly symmetric pattern of intensities in the northern section; however, south of the hypocenter, the strongest intensities are above the inclined east-dipping fault (Fig. 1) and symmetry across the surface projection of the top of the HF is broken. For this Earth model, the high GMIMs are above the fault centroid and offset from the surface projection of the fault. For the 3DTOPO Earth model, the intensities are even more asymmetric across the surface projection of the top of the fault. This is caused by differences in material properties across the fault with low wavespeed sedimentary rocks of the Great Valley
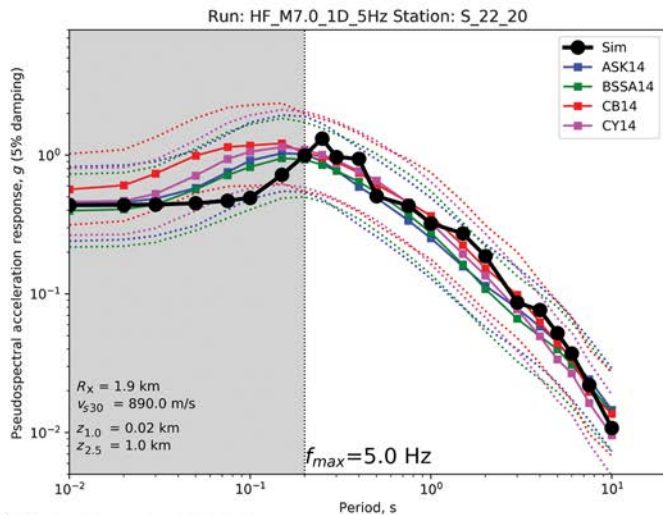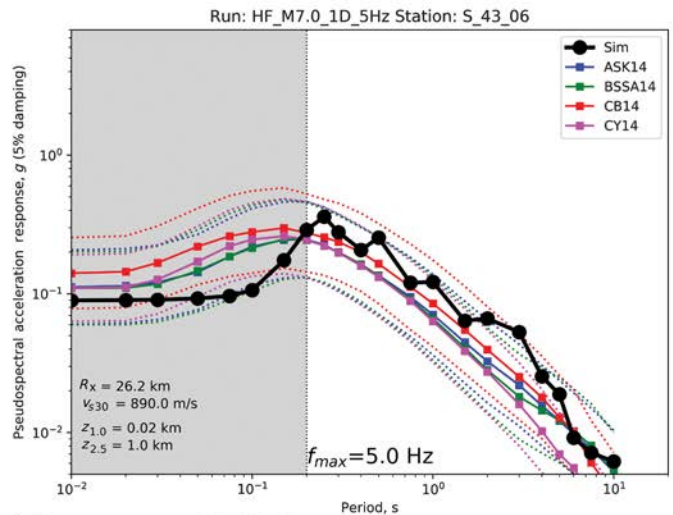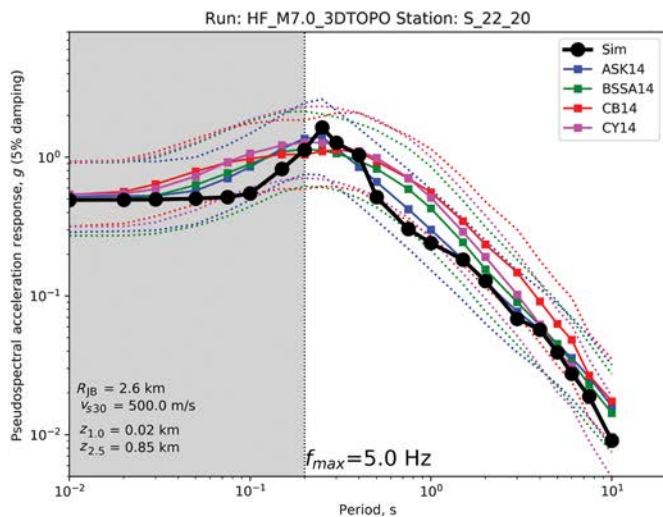
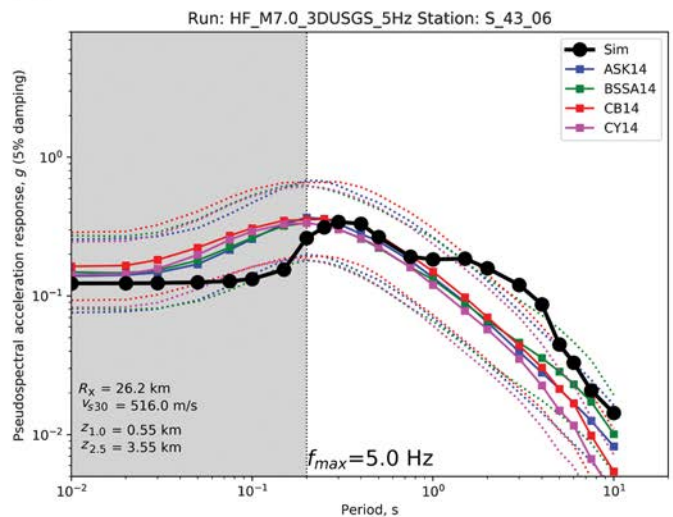▲ **Figure 5.** RotD50 spectral acceleration (SA) at two locations (circles with lines) for the 1DFLAT model in (a) Oakland and (b) Livermore and the 3DTOPO model in (c) Oakland and (d) Livermore. Predictions of SA for four ground-motion models (GMMs) are also shown (squares with lines) and uncertainties (dotted lines): Abrahamson *et al.* (2014), Boore *et al.* (2014), Campbell and Bozorgnia (2014), and Chiou and Youngs (2014). The minimum resolved period in each case (0.2 s) is shown, and the region of poorly resolved frequency response is indicated by gray shading. The color version of this figure is available only in the electronic edition.

sequence producing larger motions east of the fault and harder Franciscan rocks, resulting in lower motions west of the HF (Rodgers, Petersson, *et al.*, 2018; Rodgers, Pitarka, *et al.*, 2018). The contributions of fault geometry and the impact of our assumed minimum shear wavespeed ($V_{S\min}$) on simulated ground motions near the HF is the subject of a study being revised (A. Rodgers *et al.*, unpublished manuscript, 2019; see Data and Resources).

Finally, for comparison, we plotted the PGV map that would result from application of the Abrahamson *et al.* (2014) GMM using a 1D Earth model with constant site properties (V_{S30}, $Z_{1.0}$, and $Z_{2.5}$, Fig. 7c) and those from the USGS 3D model (Fig. 7d). PGV maps from the ASK14 GMM 1D model (Fig. 7c) show a very smooth representation of ground shaking

that depends only on the distance from the fault. Using site properties from the USGS 3D model (without $V_{S\min}$ threshold) shows that PGV values are modulated by the site conditions including strong shaking, in which V_{S30} is low (Fig. 7d). Note the differences in the spatial patterns of PGV maps from our 3DTOPO and the ASK14 GMM (Fig. 7b,d). Whereas the 3DTOPO case (Fig. 7b) has large PGV values caused by deep low wavespeed material east of the HF, the ASK14 PGV map using the USGS 3D model has large values in the near-surface low wavespeed areas west of the HF. Our physics-based simulations (Fig. 7a,b) show finer scale spatial variations than those from the ASK14 GMM because they include the effects of the variable slip distribution, fault dip, and wave propagation.
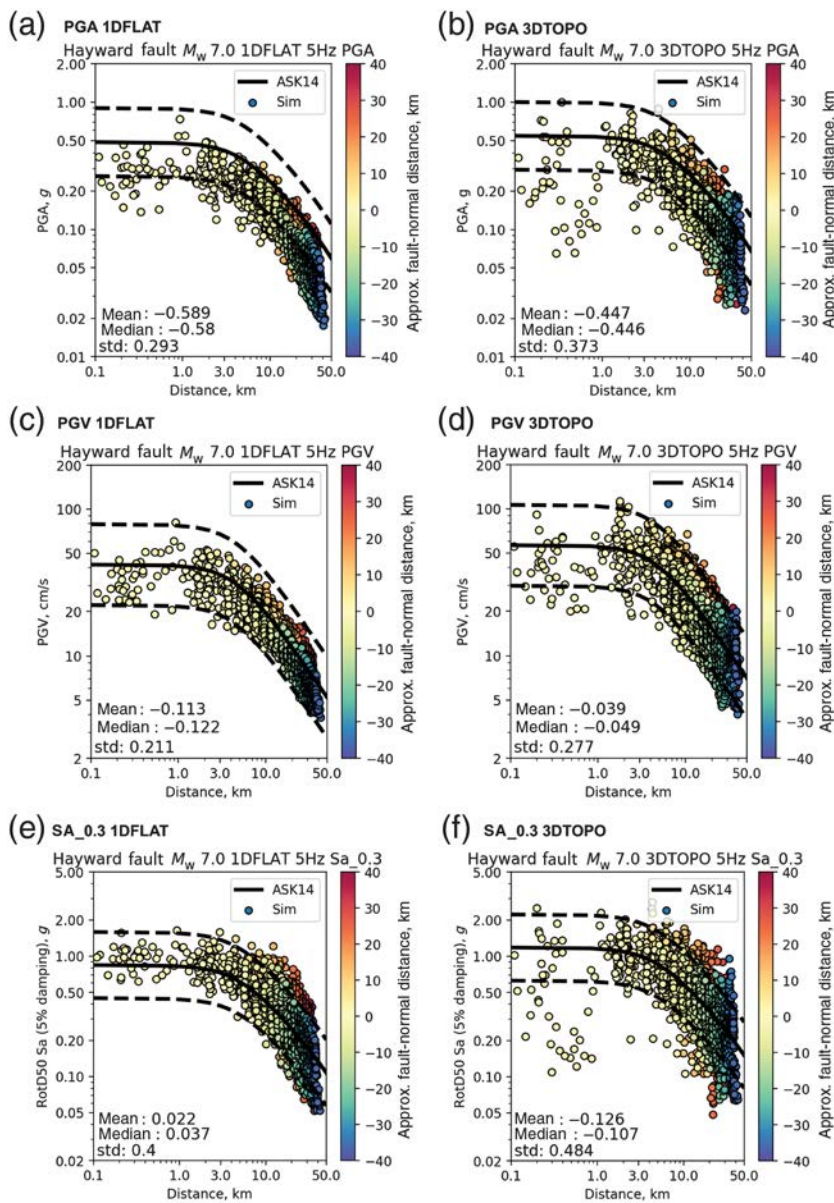
▲ **Figure 6.** Ground-motion intensity measurements (GMIMs; small circles coded by approximate fault-normal distance) versus Joyner–Boore distance for the 1DFLAT and 3DTOPO Earth models: (a,b) peak ground acceleration (PGA); (c,d) peak ground velocity (PGV); and RotD50 SA at periods: (e,f) 0.3, (g,h) 1.0, and (i, j) 3.0 s. In each panel, the predictions from the Abrahamson *et al.* (2014) GMM using the average site terms is shown (thick black lines) with 1-σ uncertainties (dashed black lines). The mean, median, and standard deviation of residuals in natural logarithm units relative to the site-specific ASK14 predictions are given in each panel. The color version of this figure is available only in the electronic edition. (*Continued*)

and boxes indicate the interquartile range (IQR, the central 50% of the data ±25% from the median). Whiskers indicate 1.5 times the IQR and outliers (absolute values > 1.5 IQR) are plotted as circles. The reported aleatory between-event uncertainties (τ) for the mean ASK14 estimates are indicated by the dashed red lines. Recall that the total variance of a GMIM estimate σ^2 is related to the sum of uncorrelated between- and within-event variances, τ^2 and ϕ^2, respectively (Al Atik *et al.*, 2010). The shortest resolved period, corresponding to $f_{\max}$ of 5.0 Hz, is 0.2 s. Therefore, SAs are likely poorly resolved for periods shorter than about 0.25 s. Across a broad range of periods, the median GMIMs (SA and PGV) are within the 1-τ uncertainties of the ASK14 GMM for both the 1DFLAT and 3DTOPO Earth models and PGA values are slightly outside this range. The 3DTOPO earth model produces more variability than the 1DFLAT model because of path and site effects. Results for these simulations are unique to the particular rupture model chosen. Different motions would result from assuming a different rupture model, fault segment and geometry, and hypocenter and slip distribution, as well as dynamic rupture properties such as rise time and stress drop. However, the good agreement between simulated GMIMs and this GMM indicates that the computed motions are consistent with empirical models and suitable for further analysis, including engineering analysis of geotechnical and structural models and earthquake early warning.

To directly compare the statistics of GMIM residuals relative to the ASK14 GMM, we plot the median and standard deviation of the ratios (Sim/GMM) for the 1DFLAT and 3DTOPO earth models on the same scale in Figure 9. We show that the median ratio is within the reported 1-τ between-event uncertainties for the ASK14 GMM (Fig. 9a). The within-event standard deviations ϕ (Fig. 9b) show that the 3DTOPO earth model consistently produces more variation (20%–75%) than the 1DFLAT earth model. This variation indicates that path and site effects due to 3D wave propagation in the USGS model cause systematic variations in the GMIMs that are not explained by the site-specific terms in the ASK14 GMM. Not surprisingly, our simulations produce within-event less variation that the ASK14 GMM because it does not draw from as diverse a population as the NGA-West2 data set.

To explore path and site effects related to 3D Earth structure, we plot maps of the site-specific properties (V_{S30}, $Z_{1.0}$, and $Z_{2.5}$) and the source-normalized intensity maps (ratio

The differences of the simulated motions relative to the site-specific ASK14 GMM predictions for all stations for both the 1DFLAT and 3DTOPO Earth models are shown in Figure 8. These show the differences as box and whisker plots for the natural logarithm of the ratio of the simulated GMIM divided by the site-specific GMM prediction for each station. The median value for each GMIM is indicated by the thick line
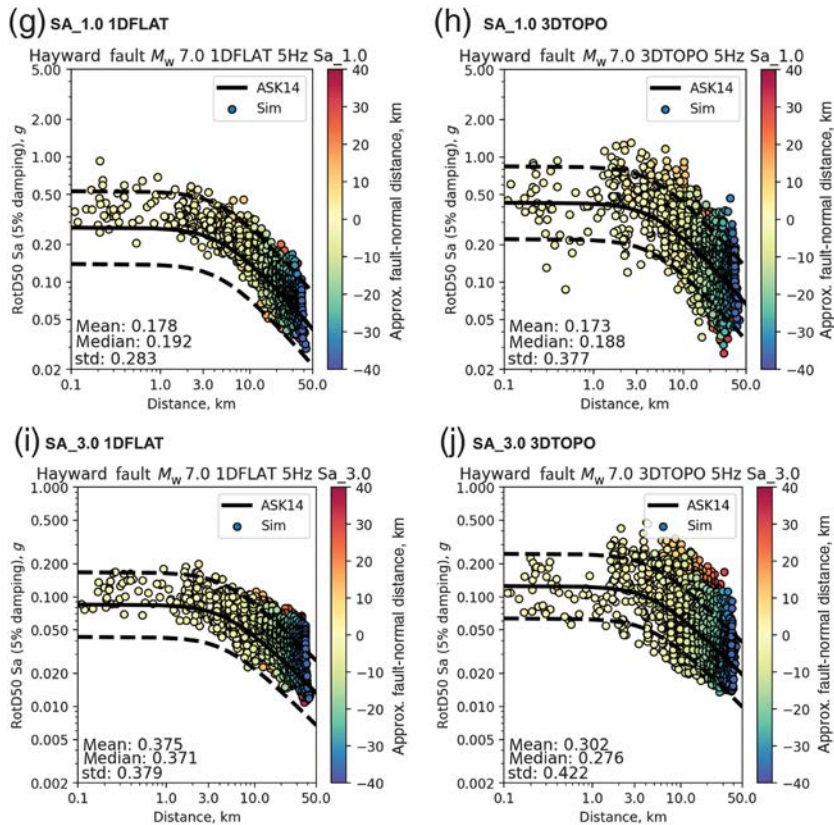
Figure 6. Continued.

of simulated GMIMs for 3DTOPO model divided by that for the 1DFLAT model). First, we present the physical properties of the 3D model. Figure 10 shows maps of site properties (2-km grid) with major geologic features labeled. For V_{S30}, we show the values from the USGS 3D model without any thresholding of shear wavespeed (Fig. 10a) as well as the V_{S30} with $V_{S\,min}$ of 500 m/s applied (Fig. 10b). The USGS 3D model has more variability in near-surface shear wavespeeds (Fig. 10a,b) than we have included in our simulations, including very low values along the East Bay shoreline, Santa Clara Valley, and parts of the San Francisco Peninsula where the ASK14 GMM produces large intensities (Fig. 7d). This indicates where our modeling can be improved by lowering $V_{S\,min}$ below 500 m/s. The $Z_{1.0}$ and $Z_{2.5}$ maps (Fig. 10c,d) indicate the deep low wavespeeds of the East Bay Hills and sedimentary basins (San Leandro basin, San Pablo Bay, Dublin–Pleasanton–Livermore Valley, the Delta, Golden Gate, La Honda, Evergreen, and Cupertino basins). Several higher elevation locations have hard-rock geology (Mount Diablo, Diablo Range, and Marin Highlands). Finally, note the very high shear wavespeeds at the surface (Fig. 10a) associated with the San Leandro Gabbro along the central HF.

Figure 11 shows maps of the natural logarithm of the ratio of four GMIMs from the 3DTOPO and 1DFLAT models (3DTOPO/1DFLAT) and plotted at each site. These are source normalized ground-motion intensity maps that quantify 3D seismic wave propagation path and site effects. It provides path- and site-specific corrections that could be applied to a GMIM

computed with a 1D Earth model to account for 3D wave propagation effects. Red and blue colors correspond to amplification and deamplification, respectively, of the 3DTOPO earth model relative to the 1DFLAT earth model. In this figure, we show maps for PGA, PGV, and RotD50 SA at 1 and 3 s. For reference, contours of the $Z_{1.0}$ map (Fig. 10c) are shown in each panel (0.2-km intervals). The PGV and RotD50 SA at 1 and 3 s GMIM ratio maps (Fig. 11b–d) are strongly correlated with geologic structure, showing higher amplitudes for the 3DTOPO model in the low wavespeed areas such as sedimentary basins (e.g., San Leandro basin, San Pablo Bay, Evergreen, Cupertino, La Honda, and Golden Gate basins and in the Delta). Deep low shear wavespeeds in the East Bay Hills result in higher amplitudes in the 3DTOPO model relative to the 1DFLAT model, similar to Rodgers, Petersson, *et al.* (2018) and Rodgers, Pitarka, *et al.* (2018) for a different rupture. Logarithmic GMIM ratios have near-zero or negative values (corresponding to near unity or lower amplitudes for the 3DTOPO earth model) in the high wavespeed areas (Mount Diablo, Diablo Range, and Marin Highlands). The PGA map (Fig. 11a) shows some correlation with geologic structure, for example, low values on the high wavespeed San Leandro Gabbro along the HF. Future simulations must lower $V_{S\,min}$ and resolve even higher frequencies to reveal effects of geotechnical properties in the USGS 3D model that shape PGA values.

Recall that the 3D Earth model produced larger variations than the 1D model (higher standard deviations, Fig. 9). In particular, the long-period GMIMs for 3DTOPO had more variation than those for 1DFLAT. Indeed, this is reflected in the maps shown in Figure 11 (note different scales). The PGV and RotD50 SA at 1 and 3 s have shown more variation than PGA. The spatial scale of variations in these GMIM ratios is also quite large and on par with scale of the geologic structure (e.g., $Z_{1.0}$) as might be expected from longer wavelength waves. The systematic variation of GMIMs for the 3DTOPO earth model and their relationship to geologic structure demonstrate how 3D wave propagation simulations can be used to understand path and site effects and explore strategies for removing systematic effects from the aleatory variability in seismic hazard analyses as recent nonergodic GMMs do based on empirical data (Lin *et al.*, 2011; Landwehr *et al.*, 2016). An important element influencing acceptance of 3D simulations for seismic hazard and risk analyses in the SFBA, such as shown herein, will be the validity of the USGS 3D model and efforts improve it.

DISCUSSION AND CONCLUSIONS

In this study, we reported ground-motion simulations for a hypothetical M_w 7.0 earthquake on the HF in the eastern
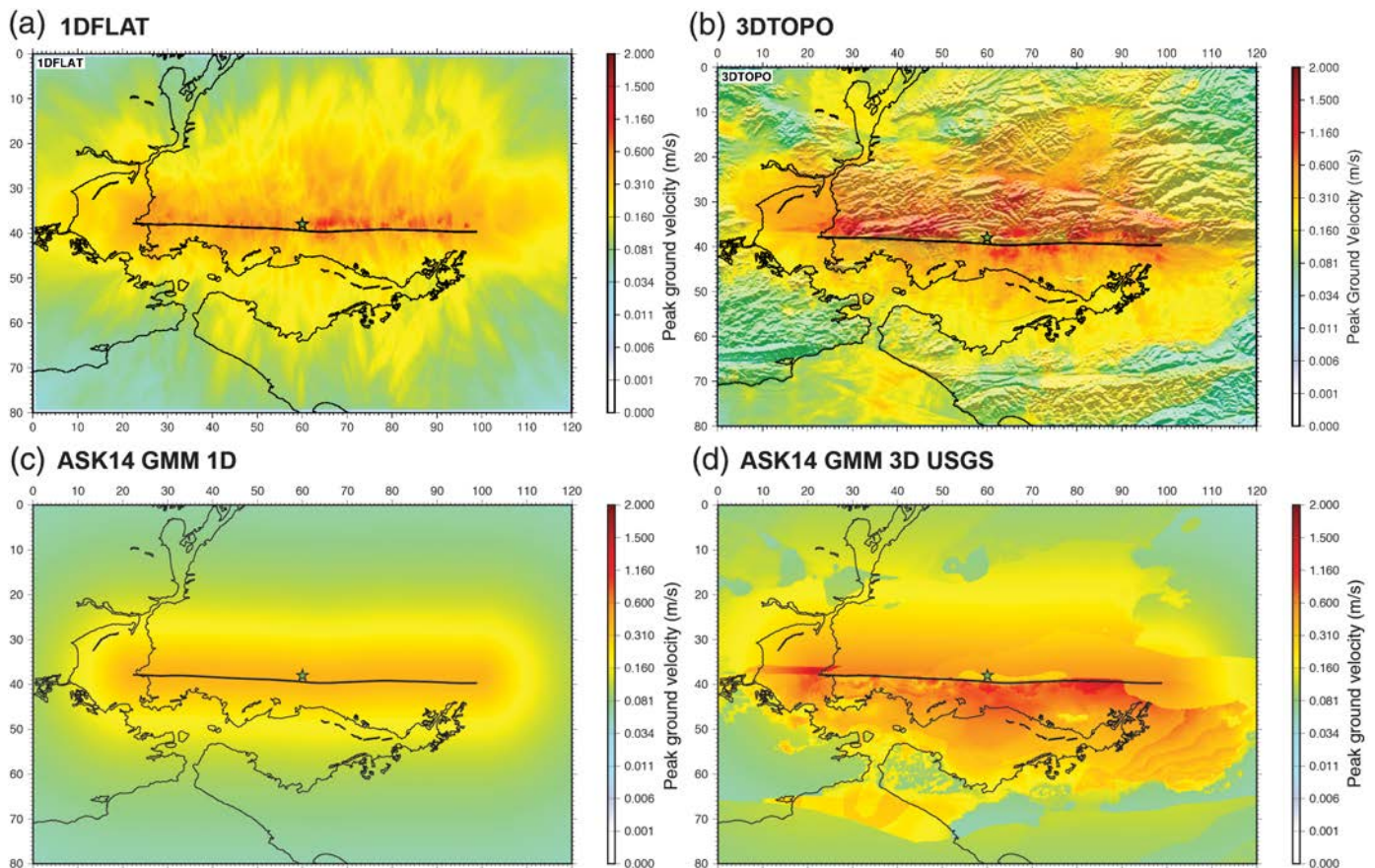
▲ **Figure 7.** Maps of the PGV (bar) at the grid resolution for different methods: (a) 1DFLAT and (b) 3DTOPO Earth models from our 3D SW4 simulations and from the ASK14 GMM assuming (c) 1D constant site parameters and (d) site parameters from the U.S. Geological Survey (USGS) 3D model. The surface projection of the top of the rupture is indicated by the thick black line and the hypocenter location is indicated by the star. The color version of this figure is available only in the electronic edition.

SFBA of northern California. We used the SW4 finite-difference code on HPC and modeled wave propagation physics in a fully 3D Earth model with topography and fine discretization to resolve frequencies of motions up to 5 Hz. This represents the highest resolution fully deterministic 3D ground-motion simulation performed in the SFBA. The 1DFLAT and 3DTOPO simulations produce GMIMs whose median values fall within the reported 1-τ uncertainties of the PEER NGA-West2 GMMs, which is a necessary condition for 3D ground motions to be acceptable for engineering applications. Path and site effects caused by wave propagation in the 3DTOPO earth model produce more variation in the ground-motion intensities than the 1DFLAT earth model. This variation is due to repeatable wave propagation effects. Future efforts to develop nonergodic GMMs (e.g., Lin *et al.*, 2011; Landwehr *et al.*, 2016) will use systematic effects such as those seen in Figure 11 so that they can be removed from path- and site-specific median ground-motion intensity estimates.

These results were made possible with advances in SW4's numerical method, algorithmic improvements, and access to HPC. SW4's mesh refinement capability enables calculation of higher frequency motions on a given computational platform. Without mesh refinement and using a fixed grid spacing,

we would achieve only about 3-Hz motions on the same computing resource. Refinement within SW4's near-surface curvilinear mesh is currently underway. The results described in this article were generated on the Cori Phase-II cluster at NERSC/LBNL using a version of SW4 optimized for efficiency on multicore (CPU) nodes. Development of a version of SW4 for graphic processing units (GPUs) is well underway, and we will report results from this code in the near future. It is expected that next-generation petaflop and exaflop computing platforms will rely heavily on GPU technologies, so this development will be key to future advancements of fully 3D seismic simulations.

The resulting ground motions are consistent with GMMs based on empirical data; specifically, the median values of GMIMs are within the between-event uncertainties (τ) of the PEER NGA-West2 models, and the within-event standard deviations (ϕ) are similar to reported values. The particular pattern of intensities for the 3DTOPO case results from both the specific rupture and 3D Earth structure. The HF dips to the east along the segment considered, and this gives rise to an asymmetry in the ground-motion intensities across the fault seen in the 1DFLAT case. Consequently, motions at a given distance from the top of the rupture for the 1DFLAT case are larger to the east and lower to the west. These results and
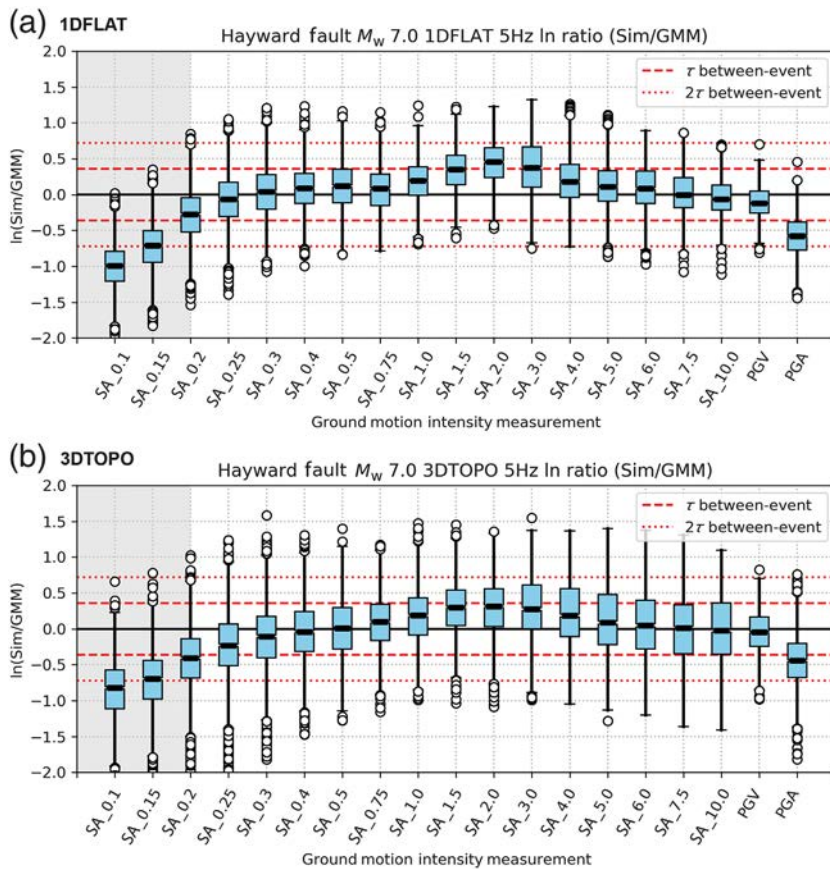
▲ **Figure 8.** Natural logarithm ratio of GMIMs as the simulation divided by ASK14 GMM prediction using site-specific terms for (a) 1DFLAT and (b) 3DTOPO Earth models. Median values for each GMIM are indicated by the thick black line and boxes indicate the interquartile range (IQR, central 50% from median). Whiskers indicate 1.5 IRQ and outliers (absolute value beyond 1.5 IQR) are shown as circles. Between-event uncertainties (τ and 2τ) for the median predictions (natural log units) are indicated by the dashed and dotted lines, respectively. Note that the shorter period SAs (SA_0.1, SA_0.15, and SA_0.2, shaded region) may be poorly resolved. The color version of this figure is available only in the electronic edition.

recent simulations of strong motions with the same 3D model (Johansen *et al.*, 2017; Rodgers, Petersson, *et al.*, 2018; Rodgers, Pitarka, *et al.*, 2018) show that for the considered frequency range (0–5 Hz), $V_{S\min}$ of 500 m/s and fully 3D wave propagation approach produce higher motions east of the HF because of fault dip and material heterogeneity. However, it should be noted that the lowest wavespeed sediments surrounding the San Francisco Bay margins provided by the USGS 3D model are not fully resolved in our simulations. A study to specifically assess the contributions of fault geometry and material heterogeneity including the impact of sediments with V_S less than the assumed $V_{S\min}$ of 500 m/s is under revision (A. Rodgers *et al.*, unpublished manuscript, 2019; see Data and Resources).

The simulations described herein promise to result in more realistic earthquake ground motions using fully deterministic 3D wave propagation physics to model higher frequencies. Such motions are based on realistic rupture models and 3D

wave propagation without the need to include high-frequency motions from 1D models or the stochastic method. As such, these simulations reveal site-to-site variations caused by 3D wave propagation. The ground motions reported here currently require world-class computing resources to resolve high frequencies of interest to engineering analyses. However, as numerical and computational methods improve and the power of HPC grows, such calculations will become easier. These calculations will run faster on modern and more widely accessible computing platforms including GPU-accelerated platforms. This can enable new computational approaches to seismic hazard and risk when motions for a wide range earthquake scenarios are simulated and assessed.

Key to this effort will be the improvement of 3D Earth models and the validation of these models against the available data. For the current study, we do not have ground-motion recordings for a large damaging event on the HF. Comparison with existing GMMs (e.g., NGA-West2) is important to building confidence in the realism of simulation results. Going forward, existing waveforms from small earthquakes can be used to evaluate and improve geologic models, as well as confirm our simulation predictions of path and site effects for these simple source events. The simulated motions shown here produce median GMIMs within the 1-σ uncertainties and standard deviations obtained from empirical data. Further consideration of interperiod correlations is needed for acceptance of simulated motions for structural response analysis (Stafford, 2017; Bayless and Abrahamson, 2018). Also important is statistical analysis of the interevent variations and partitioning of the source, path, and site variability. This will require simulation of a large suite of ruptures for a given fault segment, requiring even more computational resources.

Moderate earthquakes can be used to evaluate the current USGS 3D model of the SFBA, and these have the advantage of being simple, approximately point moment tensor sources. Previous efforts to evaluate the USGS 3D model have shown good agreement at relatively long periods, much lower frequencies than the 5 Hz considered here. Although improvements in the accuracy and resolution of the current 3D model are clearly needed, the current model represents a defensible starting point. The geometry of the major large-scale structural features (e.g., geologic–lithologic units, sedimentary basins, topography) is included. The 3D structure represented in this model reproduces the path and site effects as encoded in GMMs (including the trends reported in Rodgers, Pitarka, *et al.*, 2018). Further calculations extending the frequency content of simulations, considering a wide range of rupture models and lowering the assumed
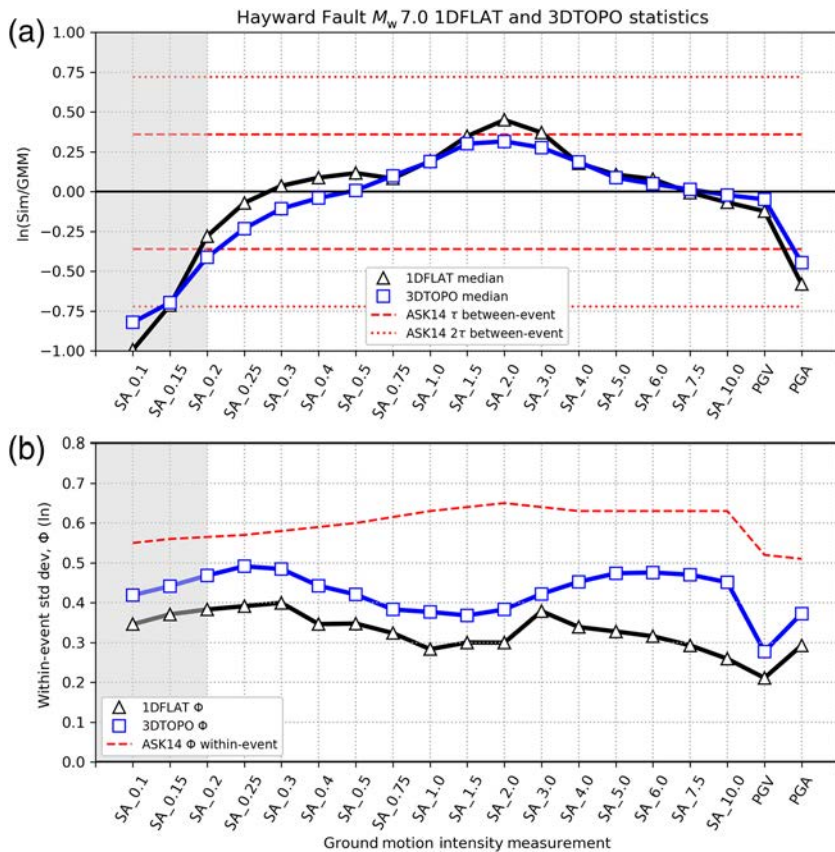
▲ **Figure 9.** Summary statistics for GMIM residuals relative to the ASK14 GMM: (a) median and (b) within-event standard deviation. All statistics are in natural logarithm units. The 1DFLAT and 3DTOPO statistics are shown as triangles and squares, respectively. Uncertainties for the ASK14 GMM are shown with broken lines for the between-event and within-event standard deviations, τ and ϕ, respectively. Note that the shorter period SAs (SA_0.1, SA_0.15, and SA_0.2, shaded region) may be poorly resolved. The color version of this figure is available only in the electronic edition.

$V_{S \min}$ will enable better understanding of systematic source, path, and site effects in the SFBA. Improved representation of path and site effects in broadband simulations and development of nonergodic GMMs can reduce uncertainties in ground-motion estimates (Lin *et al.*, 2011; Landwehr *et al.*, 2016). In addition to validation and improvement of the (median) 3D Earth model and running large suites of ruptures to capture the aleatory uncertainty in motions, understanding the epistemic uncertainty in the 3D Earth model remains a challenge to acceptance of simulated ground motions for seismic hazard. As 3D models and computational methods improve along with uncertainty estimates, motions computed with fully deterministic methods can be used to improve understanding of hazard and risk for future earthquakes, including events similar to 1868, and other previous and possible future HF ruptures.
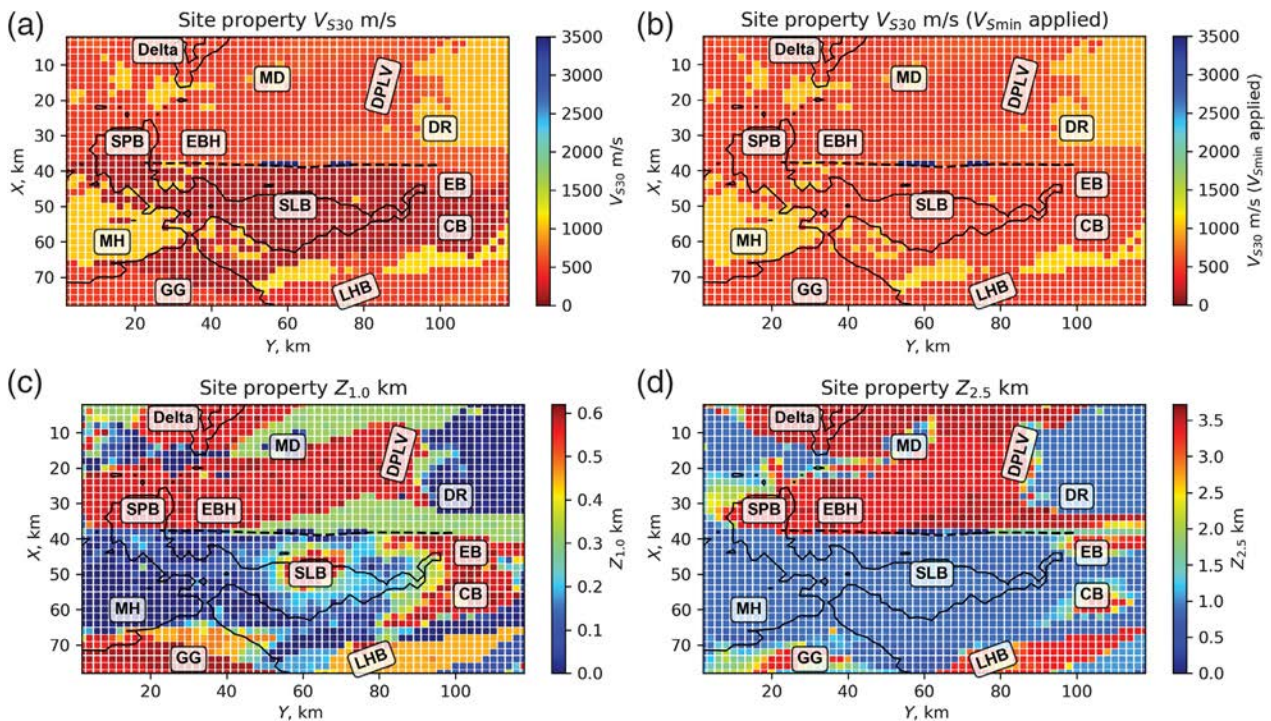
DATA AND RESOURCES

SW4 is open source and available at github.com/geodynamics/sw4 (last accessed February 2019) with assistance from the

Computational Infrastructure for Geodynamics (Petersson and Sjogreen, 2017). The rupture model was generated using the methods of Graves and Pitarka (2016) and code written by Robert Graves (U.S. Geological Survey [USGS]-Pasadena). The USGS 3D model for the San Francisco Bay area and fault geometries were obtained from the USGS website (USGS, 2018). Figures were made with the Generic Mapping Tools (GMT, Wessel *et al.*, 2013) and Python/Matplotlib. Waveforms were processed and plotted in Python with the ObsPy package (Krischer *et al.*, 2015). Ground-motion intensities and ground-motion models were computed with the pyrotd and pygmm packages, respectively, from Albert Kottke. Some processing was done with the pySW4 package from Shahar Shani-Kadmiel. An animation of the 3DTOPO simulation is available in the Ⓔ supplemental content to this article. The ground-motion time series for the 1D and 3D simulations described herein will be made available upon request. The unpublished manuscript by A. Rodgers, A. Pitarka, and D. B. McCallen (2019), "The effect of fault geometry and minimum shear wavespeed on three-dimensional ground motion simulations for an M_w 6.5 Hayward fault scenario earthquake, San Francisco Bay area, Northern California", submitted to Bull. Seismol. Soc. Am.

▲ **Figure 10.** Maps of the site-specific physical properties of the USGS 3D model: (a) V_{S30} without thresholding; (b) V_{S30} with $V_{Smin} = 500$ m/s; (c) $Z_{1.0}$; and (d) $Z_{2.5}$. In each panel, the coastline is drawn (solid lines) with the surface trace of the Hayward fault rupture considered (dashed line). Geologic features are labeled: EBH, East Bay Hills; SLB, San Leandro basin; SPB, San Pablo Bay; DPLV, Dublin–Pleasanton–Livermore Valley; MD, Mount Diablo; DR, Diablo Range; EB, Evergreen basin; CB, Cupertino basin; LHB, La Honda basin; GG, Golden Gate basin; MH, Marin Highlands. The color version of this figure is available only in the electronic edition.
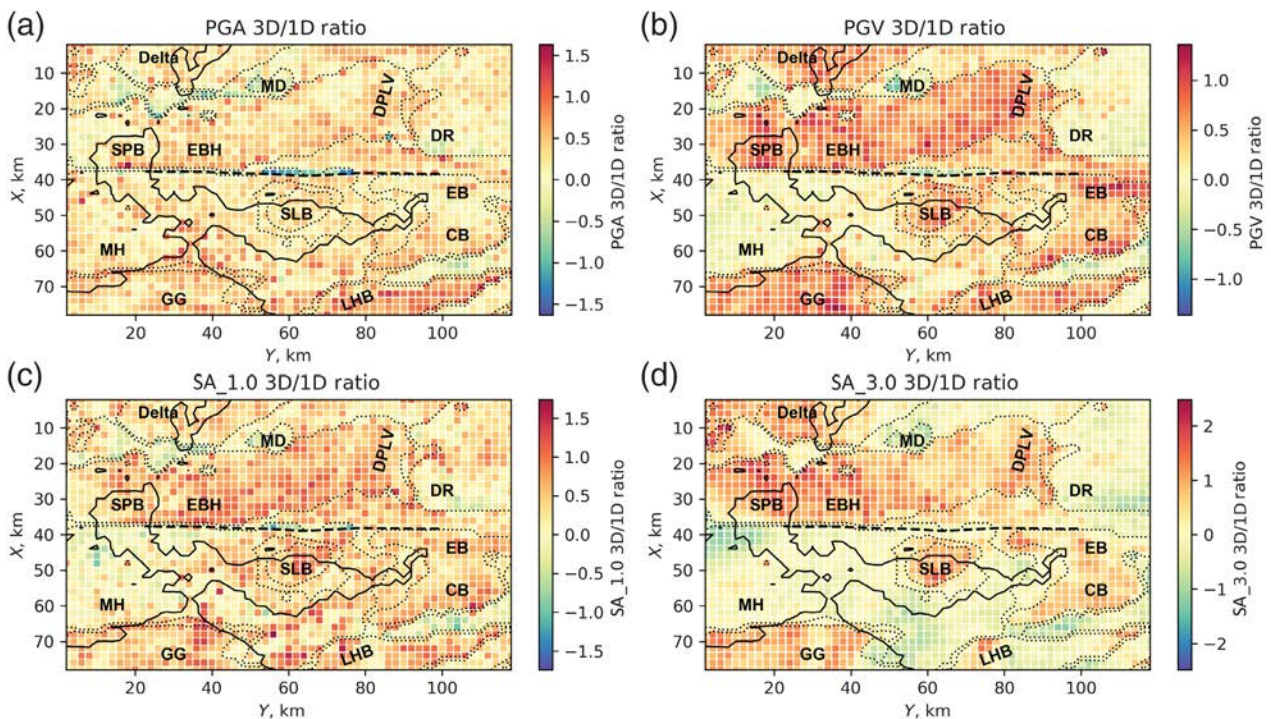
▲ **Figure 11.** Maps of the source-normalized ground-motion intensity maps (natural logarithm of intensity ratios, 3DTOPO/1DFLAT): (a) PGA, (b) PGV, (c) RotD50 SA at 1 s, and (d) RotD50 SA at 3 s (note different scales). In each panel, the coastline is drawn (solid lines) with the surface trace of the Hayward fault rupture considered (dashed line) and contours of the $Z_{1.0}$ (0.2-km interval, black dotted lines). Geologic features are labeled as in Figure 10. The color version of this figure is available only in the electronic edition.

REFERENCES

Aagaard, B. T., T. M. Brocher, D. Dolenc, D. Dreger, R. W. Graves, S. Harmsen, S. Hartzell, S. Larsen, K. McCandless, S. Nilsson, *et al.* (2008). Ground-motion modeling of the 1906 San Francisco earthquake, part II: Ground-motion estimates for the 1906 earthquake and scenario events, *Bull. Seismol. Soc. Am.* **98,** no. 2, 1012–1046, doi: 10.1785/0120060410.

Aagaard, B. T., R. W. Graves, A. Rodgers, T. M. Brocher, R. W. Simpson, D. Dreger, N. A. Petersson, S. C. Larsen, S. Ma, and R. C. Jachens (2010). Ground motion modeling of Hayward fault scenario earthquakes, part II: Simulation of long-period and broadband ground motions, *Bull. Seismol. Soc. Am.* **100,** no. 6, 2945–2977, doi: 10.1785/0120090379.

Abrahamson, N. A., W. J. Silva, and R. Kamai (2014). Summary of the ASK14 ground motion relation for active crustal regions, *Earthq. Spectra* **30,** no. 3, 1025–1055, doi: 10.1193/070913EQS198M.

Afanasiev, M., C. Boehm, M. van Driel, L. Krischer, M. Rietmann, D. A. May, M. G. Knepley, and A. Fichtner (2018). Modular and flexible spectral-element waveform modelling in two and three dimensions, *Geophys. J. Int.* **216,** no. 3, 1675–1692, doi: 10.1093/gji/ggy469.

Al Atik, L., N. Abrahamson, J. J. Bommer, F. Scherbaum, F. Cotton, and N. Kuehn (2010). The variability of ground-motion prediction models and its components, *Seismol. Res. Lett.* **81,** no. 5, 794–801, doi: 10.1785/gssrl.81.5.794.

Anderson, J. G., and J. N. Brune (1999). Probabilistic seismic hazard analysis without the ergodic assumption, *Seismol. Res. Lett.* **70,** no. 1, 19–28.

Bakun, W. H. (1999). Seismic activity of the San Francisco Bay region, *Bull. Seismol. Soc. Am.* **89,** no. 3, 764–784.

Bao, H., J. Bielak, O. Ghattas, L. F. Kallivokas, D. R. O'Hallaron, J. R. Shewchuk, and J. Xu (1998). Large-scale simulation of elastic wave propagation in heterogeneous media on parallel computers, *Comput. Methods Appl. Mech. Eng.* **152,** 85–102.

Bayless, J., and N. Abrahamson (2018). Implications of the inter-period correlation of strong ground motions on structural risk, *Proc. of the 11th National Conf. on Earthquake Engineering*, Earthquake Engineering Research Institute, Los Angeles, 25–29 June 2018, Paper ID 611.

Bielak, J., R. W. Graves, K. B. Olsen, R. Taborda, L. Ramírez-Guzmán, S. M. Day, G. P. Ely, D. Roten, T. H. Jordan, P. J. Maechling, *et al.* (2010). The ShakeOut earthquake scenario: Verification of three simulation sets, *Geophys. J. Int.* **180,** no. 1, 375–404.

Boatwright, J., and H. Bundock (2008). Modified Mercalli intensity maps for the 1868 Hayward earthquake plotted in ShakeMap format, *U.S. Geol. Surv. Open-File Rept. 2008-1121*, available at https://pubs.usgs.gov/of/2008/1121/ (last accessed February 2019).

Bonilla, L. F., R. J. Archuleta, and D. Lavallée (2005). Hysteretic and dilatant behavior of cohesionless soils and their effects on nonlinear site response: Field data, observations and modeling, *Bull. Seismol. Soc. Am.* **95,** 2373–2395.

Boore, D. M. (1972). Finite difference methods for seismic wave propagation in heterogeneous materials, in *Methods in Computational Physics: Advances in Research and Applications*, Vol. 11, Seismology: Surface waves and Earth oscillations, B. A. Bolt (Editor), Academic Press, 1–37.

Boore, D. M. (1983). Stochastic simulation of high-frequency ground motions based on seismological models of the radiated spectra, *Bull. Seismol. Soc. Am.* **73,** 1865–1894.

Boore, D. M. (2003). Simulation of ground motion using the stochastic method, *Pure Appl. Geophys.* **160,** 635–676.

Boore, D. M. (2010). Orientation independent, nongeometric-mean measures of seismic intensity from two horizontal components of motion, *Bull. Seismol. Soc. Am.* **100,** 1830–1835.

Boore, D. M., J. P. Stewart, E. Seyhan, and G. M. Atkinson (2014). NGA-West2 equations for predicting PGA, PGV, and 5% damped PSA for shallow crustal earthquakes, *Earthq. Spectra* **30,** 1057–1085.

Boore, D. M., J. Watson-Lamprey, and N. A. Abrahamson (2006). Orientation-independent measures of ground motion, *Bull. Seismol. Soc. Am.* **96,** no. 4A, 1502–1511.

Bouchon, M. (1981). A simple method to calculate Green's functions for elastic layered media, *Bull. Seismol. Soc. Am.* **71,** no. 4, 959–971.

Campbell, K. W., and Y. Bozorgnia (2014). NGA-West2 ground motion model for the average horizontal components of PGA, PGV, and 5% damped linear acceleration response spectra, *Earthq. Spectra* **30,** 1087–1115.

Chaljub, E., D. Komatitsch, J.-P. Vilotte, Y. Capdeville, B. Valette, and G. Festa (2007). Spectral element analysis in seismology, in *Advances in Wave Propagation in Heterogeneous Media: Advances in Geophysics*, R.-S. Wu and V. Maupin (Editors), Elsevier Academic Press, London, United Kingdom, 365–419.

Chaljub, E., P. Moczo, S. Tsuno, P.-Y. Bard, J. Kristek, M. Kaser, M. Stupazzini, and M. Kristekova (2010). Quantitative comparison of four numerical predictions of 3D ground motion in the Grenoble Valley, France, *Bull. Seismol. Soc. Am.* **100,** no. 4, 1427–1455.

Chiou, B. S.-J., and R. R. Youngs (2014). Update of the Chiou and Youngs NGA model for the average horizontal component of peak ground motion and response spectra, *Earthq. Spectra* **30,** 1117–1153.

Crempien, J. G. F., and R. J. Archuleta (2015). UCSB method for simulation of broadband ground motion from kinematic earthquake sources, *Seismol. Res. Lett.* **86,** no. 1, doi: 10.1785/0220140103.

Cui, Y., E. Poyraz, K. B. Olsen, J. Zhou, K. Withers, S. Callaghan, J. Larkin, C. Guest, D. Choi, A. Chourasia, *et al.* (2013). Physics-based seismic hazard analysis on petascale heterogeneous supercomputers, *Proc. of Supercomputing Conference*, Denver, Colorado, 17–22 November 2013.

Day, S. M., R. W. Graves, J. Bielak, D. S. Dreger, S. Larsen, K. B. Olsen, A. Pitarka, and L. Ramirez-Guzman (2008). Model for basin effect on long-period response spectra in southern California, *Earthq. Spectra* **24,** 257–277.

Dreger, D. S., M.-H. Huang, A. Rodgers, T. Taira, and K. Wooddell (2015). Kinematic finite-source model for the 24 August 2014 South Napa, California earthquake from joint inversion of seismic, GPS and InSAR data, *Seismol. Res. Lett.* **86,** no. 2A, doi: 10.1785/0220140244.

Dumbser, M., and M. Käser (2006). An arbitrary high-order discontinuous Galerkin method for elastic waves on unstructured meshes—II. The three-dimensional isotropic case, *Geophys. J. Int.* **167,** no. 1, 319–336, doi: 10.1111/j.1365-246X.2006.03120.x.

Etienne, V., E. Chaljub, J. Virieux, and N. Glinsky (2010). An hp-adaptive discontinuous Galerkin finite-element method for 3-D elastic wave modelling, *Geophys. J. Int.* **183,** no. 2, 941–962.

Field, E. H., and 2014 Working Group on California Earthquake Probabilities, (2015). UCERF3: A new earthquake forecast for California's complex fault system, *U.S. Geol. Surv. 2015–3009*, 6 pp., doi: 10.3133/fs20153009.

Frankel, A., W. Stephenson, and D. Carver (2009). Sedimentary basin effects in Seattle, Washington: Ground-motion observations and 3D simulations, *Bull. Seismol. Soc. Am.* **99,** 1579–1611, doi: 10.1785/0120080203.

Furumura, T., B. L. N. Kennett, and H. Takenaka (1998). Parallel 3-D pseudospectral simulation of seismic wave propagation, *Geophysics* **63,** no. 1, 279–288, doi: 10.1190/1.1444322.

Graves, R., and A. Pitarka (2015). Refinements to the Graves and Pitarka (2010) broadband ground-motion simulation method, *Seismol. Res. Lett.* **86,** doi: 10.1785/0220140101.

Graves, R., and A. Pitarka (2016). Kinematic ground-motion simulations on rough faults including effects of 3D stochastic velocity perturbations, *Bull. Seismol. Soc. Am.* **106,** no. 5, 2136–2153, doi: 10.1785/0120160088.

Graves, R. W. (1996). Simulating seismic wave propagation in 3D elastic media using staggered-grid finite differences, *Bull. Seismol. Soc. Am.* **86,** 1091–1106.

Graves, R. W., and A. Pitarka (2010). Broadband ground-motion simulation using a hybrid approach, *Bull. Seismol. Soc. Am.* **100,** 2095–2123, doi: 10.1785/0120100057.

Graves, R. W., B. T. Aagaard, K. W. Hudnut, L. M. Star, J. P. Stewart, and T. H. Jordan (2008). Broadband simulations for M_w 7.8 southern San Andreas earthquakes: Ground motion sensitivity to rupture speed, *Geophys. Res. Lett.* **35,** no. 22, doi: 10.1029/2008GL035750.

Graves, R. W., A. Pitarka, and P. G. Somerville (1998). Ground-motion amplification in the Santa Monica area: Effects of shallow basin-edge structure, *Bull. Seismol. Soc. Am.* **88,** no. 5, 1224–1242.

Hanks, T. C., and R. K. McGuire (1981). The character of high-frequency strong ground motion, *Bull. Seismol. Soc. Am.* **71,** no. 6, 2071–2095.

Hardebeck, J. L., A. J. Michael, and T. M. Brocher (2007). Seismic velocity structure and seismotectonics of the eastern San Francisco Bay region, California, *Bull. Seismol. Soc. Am.* **97,** no. 3, 826–842, doi: 10.1785/0120060032.

Harmsen, S., S. Hartzell, and P. Liu (2008). Simulated ground motion in Santa Clara Valley, California, and vicinity from M ≥ 6.7 scenario earthquakes, *Bull. Seismol. Soc. Am.* **98,** no. 3, 1243–1271, doi: 10.1785/0120060230.

Hartzell, S., L. F. Bonilla, and R. A. Williams (2004). Prediction of nonlinear soil effects, *Bull. Seismol. Soc. Am.* **94,** 1609–1629.

Hartzell, S., S. Harmsen, and A. Frankel (2010). Effects of 3D random correlated velocity perturbations on predicted ground motions, *Bull. Seismol. Soc. Am.* **100,** 1415–1426.

Hirakawa, E., A. Pitarka, and R. Mellors (2016). Generation of shear motion from an isotropic explosion source by scattering in heterogeneous media, *Bull. Seismol. Soc. Am.* **106,** no. 5, 2313–2319, doi: 10.1785/0120150243.

Hough, S. E., and S. S. Martin (2015). The 1868 Hayward fault, California, earthquake: Implications for earthquake scaling relations on partially creeping faults, *Bull. Seismol. Soc. Am.* **105,** no. 6, 2894–2909, doi: 10.1785/0120140372.

Igel, H. (1999). Wave propagation in spherical sections by the Chebyshev spectral method, *Geophys. J. Int.* **136,** no. 3, 559–566.

Johansen, H., A. Rodgers, N. A. Petersson, D. McCallen, B. Sjogreen, and M. Miah (2017). Toward exascale earthquake ground motion simulations for near-fault engineering analysis, *Comput. Sci. Eng.* **19,** 27–37, doi: 10.1109/MCSE.2017.3421558.

Kamai, R., N. Abrahamson, and R. Graves (2014). Adding fling effects to processed ground-motion time histories, *Bull. Seismol. Soc. Am.* **104,** no. 4, doi: 10.1785/0120130272.

Käser, M., and M. Dumbser (2005). An arbitrary high order discontinuous Galerkin method for elastic waves on unstructured meshes – I: The two-dimensional isotropic case with external source terms, *Geophys. J. Int.* **166,** 855–877, doi: 10.1111/j.1365-246X.2006.03051.x.

Kawase, H. (1996). The cause of the damage belt in Kobe: "The basin-edge effect," constructive interference of the direct S-wave with the basin-induced diffracted/Rayleigh waves, *Seismol. Res. Lett.* **67,** no. 5, 25–34, doi: 10.1785/gssrl.67.5.25.

Kim, A., D. S. Dreger, and S. Larsen (2010). Moderate earthquake ground-motion validation in the San Francisco Bay area, *Bull. Seismol. Soc. Am.* **100,** 819–825.

Komatitsch, D., and J. Tromp (1999). Introduction to the spectral element method for three-dimensional seismic wave propagation, *Geophys. J. Int.* **139,** no. 3, 806–822, doi: 10.1046/j.1365-246x.1999.00967.x.

Komatitsch, D., S. Tsuboi, and J. Tromp (2005). The spectral-element method in seismology, in *Seismic Earth: Array Analysis of Broadband Seismograms*, A. Levander and G. Nolet (Editors), Vol. 157, AGU Monograph, doi: 10.1029/157GM13.

Krischer, L., T. Megies, R. Barsch, M. Beyreuther, T. Lecocq, C. Caudron, and J. Wassermann (2015). ObsPy: A bridge for seismology into the scientific Python ecosystem, *Comput. Sci. Discov.* **8,** no. 1, 14,003–14,020, doi: 10.1088/1749-4699/8/1/014003.

Landwehr, N., N. M. Kuehn, T. Scheffer, and N. Abrahamson (2016). A nonergodic ground-motion model for California with spatially varying coefficients, *Bull. Seismol. Soc. Am.* **106,** no. 6, 2574–2583, doi: 10.1785/0120160118.

Larsen, S. C., D. Dreger, M. Antolik, and C. Stidham (2000). 3-D simulations of scenario earthquake along the Hayward fault, *Technical Report UCRL-ID-137645*, Lawrence Livermore National Laboratory, 8 pp.

Levander, A. R. (1988). Fourth-order finite-difference P-SV seismograms, *Geophysics* **53,** 1425–1436.

Lienkaemper, J. J., T. E. Dawson, S. F. Personius, G. G. Seitz, L. M. Reidy, and D. P. Schwartz (2002). A record of large earthquakes on the southern Hayward fault for the past 500 years, *Bull. Seismol. Soc. Am.* **92,** no. 7, 2637–2658.

Lienkaemper, J. J., P. L. Williams, and T. P. Guilderson (2010). Evidence for a twelfth large earthquake on the southern Hayward fault in the past 1900 years, *Bull. Seismol. Soc. Am.* **100,** no. 5A, 2024–2034, doi: 10.1785/0120090129.

Lin, P.-S., B. Chiou, N. Abrahamson, M. Walling, C. T. Lee, and C.-T. Cheng (2011). Repeatable source, site, and path effects on the standard deviation for empirical ground-motion prediction models, *Bull. Seismol. Soc. Am.* **101,** no. 5, 2281–2295, doi: 10.1785/0120090312.

Moczo, P., J. Kristek, and M. Galis (2014). *The Finite-Difference Modeling of Earthquake Ground Motions: Waves and Rupture*, Cambridge University Press, Cambridge, United Kingdom.

Moczo, P., J. Kristek, M. Galis, E. Chaljub, and V. Etienne (2011). 3-D finite-difference, finite-element, discontinuous-Galerkin and spectral-element schemes analyzed for their accuracy with respect to P-wave to S-wave speed ratio, *Geophys. J. Int.* **187,** no. 3, 1645–1667, doi: 10.1111/j.1365-246X.2011.05221.x.

Nilsson, S., N. A. Petersson, B. Sjögreen, and H.-O. Kreiss (2007). Stable difference approximations for the elastic wave equation in second order formulation, *SIAM J. Numer. Anal.* **45,** 1902–1936, doi: 10.1137/060663520.

Olsen, K., and R. Takedatsu (2015). The SDSU broadband ground-motion generation module BBtoolbox Version 1.5, *Seismol. Res. Lett.* **86,** no. 1, doi: 10.1785/0220140102.

Olsen, K. B. (2000). Site amplification in the Los Angeles basin from three-dimensional modeling of ground motion, *Bull. Seismol. Soc. Am.* **90,** S77–S94.

Olsen, K. B., R. J. Archuleta, and J. Matarese (1995). Three-dimensional simulation of a magnitude 7.75 earthquake on the San Andreas fault, *Science* **270,** 1628–1632.

Olsen, K. B., S. M. Day, L. A. Dalguer, J. Mayhew, Y. Cui, J. Zhu, V. M. Cruz-Atienza, D. Roten, P. Maechling, T. H. Jordan, *et al.* (2009). ShakeOut-D: Ground motion estimates using an ensemble of large earthquakes on the southern San Andreas fault with spontaneous rupture propagation, *Geophys. Res. Lett.* **36,** L04303, doi: 10.1029/2008GL036832.

Olsen, K. B., S. M. Day, J. B. Minster, Y. Cui, A. Chourasia, M. Faerman, R. Moore, P. Maechling, and T. Jordan (2006). Strong shaking in Los Angeles expected from southern San Andreas earthquake, *Geophys. Res. Lett.* **33,** L07305, doi: 10.1029/2005GL025472.

Peter, D., D. Komatitsch, Y. Luo, R. Martin, N. Le Go, E. Casarotti, P. Le Loher, F. Magnoni, Q. Liu, C. Blitz, *et al.* (2011). Forward and adjoint simulations of seismic wave propagation on fully unstructured hexahedral meshes, *Geophys. J. Int.* **186,** no. 2, 721–739.

Petersson, N. A., and B. Sjogreen (2010). Reference guide to WPP version 2.0, *Tech. Rep. LLNL-TR-422928*, Lawrence Livermore Natl. Lab., Livermore, California.

Petersson, N. A., and B. Sjögreen (2012). Stable and efficient modeling of anelastic attenuation in seismic wave propagation, *Comm. Comput. Phys.* **12,** no. 1, 193–225, doi: 10.4208/cicp.201010.090611a.

Petersson, N. A., and B. Sjogreen (2014). Super-grid modeling of the elastic wave equation in semi-bounded domains, *Comm. Comput. Phys.* **16,** 913–955.

Petersson, N. A., and B. Sjogreen (2015). Wave propagation in anisotropic elastic materials and curvilinear coordinates using a summation-by-parts finite difference method, *J. Comp. Phys.* **299,** 820–841, doi: 10.1016/j.jcp.2015.07.023.

Petersson, N. A., and B. Sjogreen (2017). Geodynamics/SW4, Version 2.01 [software], Zenodo, doi: 10.5281/zenodo.1063644.

Petersson, N. A., and B. E. Sjogreen (2018). *SW4 Users Guide, Version 2.01*, Lawrence Livermore National Laboratory, LLNL-SM–741439.

Pitarka, A. (1999). 3D elastic finite difference modeling of seismic wave propagation using staggered grid with non-uniform spacing, *Bull. Seismol. Soc. Am.* **88,** 54–68.

Pitarka, A., R. J. Mellors, W. R. Walter, S. Ezzedine, O. Vorobiev, T. Antoun, J. L. Wagoner, E. M. Matzel, S. R. Ford, A. J. Rodgers, *et al.* (2015). Analysis of ground motion from an underground chemical explosion, *Bull. Seismol. Soc. Am.* **105,** no. 5, 2390–2410, doi: 10.1785/0120150066.

Pitarka, A., P. G. Somerville, Y. Fukushima, T. Uetake, and K. Irikura (2000). Simulation of near-fault strong-ground motion using hybrid Green's functions, *Bull. Seismol. Soc. Am.* **90,** 566–586.

Pitarka, A., H. K. Thio, P. Somerville, and L. F. Bonilla (2013). Broadband ground-motion simulation of an intraslab earthquake and nonlinear site response: 2010 Ferndale, California, earthquake case study, *Seismol. Res. Lett.* **84,** no. 5, 785–795, doi: 10.1785/0220130031.

Rodgers, A., N. A. Petersson, S. Nilsson, B. Sjogreen, and K. McCandless (2008). Broadband waveform modeling of moderate earthquakes in the San Francisco Bay area and preliminary assessment of the USGS 3D seismic velocity model, *Bull. Seismol. Soc. Am.* **98,** 969–988, doi: 10.1785/0120060407.

Rodgers, A., N. A. Petersson, A. Pitarka, and D. Mccallen (2018). Simulation of large scenario and recorded moderate earthquakes in the San Francisco Bay area, *Proc. of the 11th National Conf. on Earthquake Engineering*, Earthquake Engineering Research Institute, Los Angeles, 25–29 June 2018, Paper ID 366.

Rodgers, A. J., N. A. Petersson, and B. Sjogreen (2010). Simulation of topographic effects on seismic waves from shallow explosions near the North Korean nuclear test site with emphasis on shear wave generation, *J. Geophys. Res.* **115,** no. B11309, doi: 10.1029/2010JB007707.

Rodgers, A. J., A. Pitarka, N. A. Petersson, B. Sjogreen, and D. McCallen (2018). Broadband (0–4 Hz) ground motions for a magnitude 7.0 Hayward fault earthquake with 3D structure and topography, *Geophys. Res. Lett.* **45,** 739–747, doi: 10.1002/2017GL076505.

Sjogreen, B., and N. A. Petersson (2012). A fourth order accurate finite difference scheme for the elastic wave equation in second order formulation, *J. Sci. Comput.* **52,** no. 1, 17–48, doi: 10.1007/s10915-011-9531-1.

Stafford, P. J. (2017). Interfrequency correlations among Fourier spectral ordinates and implications for stochastic ground-motion simulation, *Bull. Seismol. Soc. Am.* **107,** no. 6, 2774–2791, doi: 10.1785/0120170081.

Taborda, R., and J. Bielak (2011). Large-scale earthquake simulation: Computational seismology and complex engineering systems, *Comput. Sci. Eng.* **13,** 14–26, doi: 10.1109/MCSE.2011.19.

Taborda, R., and J. Bielak (2013). Ground-motion simulation and validation of the 2008 Chino Hills, California, earthquake, *Bull. Seismol. Soc. Am.* **103,** no. 1, 131–156.

Taborda, R., S. Azizzadeh-Roodpish, N. Khoshnevis, and K. Cheng (2016). Evaluation of the southern California seismic velocity models through simulation of recorded events, *Geophys. J. Int.* **205,** no. 3, 1342–1364, doi: 10.1093/gji/ggw085.

Tape, C., Q. Liu, A. Maggi, and J. Tromp (2009). Adjoint tomography of the southern California crust, *Science* **325,** 988–992, doi: 10.1126/science.1175298.

Toppozada, T. R., D. M. Branum, M. S. Reichle, and C. L. Hallstrom (2002). San Andreas fault zone, California; M ≥ 5 : 5 earthquake history, *Bull. Seismol. Soc. Am.* **92,** no. 7, 2555–2601.

Toppozada, T. R., C. R. Real, and D. L. Parke (1981). Preparation of isoseismal maps and summaries of reported effects for Pre-1900 California earthquakes, *Calif. Div. Mines Geol. Open-File Rept. 81-11 SAC*, 182 pp.

Tu, T., H. Yu, L. Ramirez-Guzman, J. Bielak, O. Ghabas, K. L. Ma, and D. R. O'Hallaron (2006). From mesh generation to scientific visualization: An end-to-end approach to parallel supercomputing, *Proc. of the 2006 ACM/IEEE Conf. on Supercomputing*, Assocation for Computing Machinary, New York, New York, 91.

U.S. Geologic Survey (2018). 3-D geologic and seismic velocity models of the San Francisco Bay region, available at https://earthquake.usgs.gov/data/3dgeologic (last accessed February 2019).

Vidale, J. E., and D. V. Helmberger (1988). Elastic finite-difference modeling of the 1971 San Fernando, California earthquake, *Bull. Seismol. Soc. Am.* **78,** no. 1, 122–141.

Virieux, J. (1986). P-SV wave propagation in heterogeneous media: Velocity-stress finite-difference method, *Geophysics* **51,** 889–901.

Waldhauser, F., and W. L. Ellsworth (2002). Fault structure and mechanics of the Hayward fault, California, from double-difference earthquake locations, *J. Geophys. Res.* **107,** no. B3, doi: 10.1029/2000JB000084.

Waldhauser, F., and D. P. Schaff (2008). Large-scale relocation of two decades of northern California seismicity using cross-correlation and double-difference methods, *J. Geophys. Res.* **113,** no. B08311, doi: 10.1029/2007JB005479.

Wenk, S., C. Pelties, H. Igel, and M. Käser (2013). Regional wave propagation using the discontinuous Galerkin method, *Solid Earth* **4,** 43–57, doi: 10.5194/se-4-43-2013.

Wessel, P., W. H. F. Smith, R. Scharroo, J. F. Luis, and F. Wobbe (2013). Generic Mapping Tools: Improved version released, *Eos Trans. AGU* **94,** 409–410.

Yu, E., and P. Seagall (1996). Slip in the 1868 Hayward earthquake from the analysis of historical triangulation data, *J. Geophys. Res.* **101,** no. 7, 16,101–16,118.

Zhu, L., and L. A. Rivera (2002). A note on the dynamic and static displacements from a point source in multi-layered media, *Geophys. J. Int.* **148,** 619–627, doi: 10.1046/j.1365-246X.2002.01610.x.

Arthur J. Rodgers[1,2]
Arben Pitarka
Atmospheric, Earth and Energy Division and Geophysical Monitoring Program
Lawrence Livermore National Laboratory
7000 East Avenue, L-046
Livermore, California 94551 U.S.A.
rodgers7@llnl.gov

N. Anders Petersson
Bjorn Sjogreen
Center of Applied Scientific Computing
Lawrence Livermore National Laboratory
7000 East Avenue, L-561
Livermore, California 94551 U.S.A.

David B. McCallen[1]
University of Nevada
1644 North Virginia Street
Reno MS 0258
Reno, Nevada 89577-0258 U.S.A.

Norman Abrahamson
Department of Civil and Enviornmental Engineering
University of California, Berkeley
455 Davis Hall
Berkeley, California 94720-1710 U.S.A.

Published Online 27 February 2019

[1] Also at Earth and Environmental Sciences Area, Lawrence Berkeley National Laboratory, 1 Cyclotron Road, MS74R316C, Berkeley, California 94720 U.S.A.

[2] Also at Berkeley Seismological Laboratory, University of California, Berkeley, 307 McCone Hall #4760, Berkeley, California 94720-4760 U.S.A.